J. Fluid Mech. (2016), *vol.* 790, *pp.* 453–491. © Cambridge University Press 2016
doi:10.1017/jfm.2016.19

Numerical investigation of near-wake characteristics of cavitating flow over a circular cylinder

Aswin Gnanaskandan[1] **and Krishnan Mahesh**[1,†]

[1]Department of Aerospace Engineering and Mechanics, University of Minnesota, Minneapolis, MN 55455, USA

(Received 9 April 2015; revised 10 December 2015; accepted 6 January 2016)

A homogeneous mixture model is used to study cavitation over a circular cylinder at two different Reynolds numbers ($Re = 200$ and 3900) and four different cavitation numbers ($\sigma = 2.0$, 1.0, 0.7 and 0.5). It is observed that the simulated cases fall into two different cavitation regimes: cyclic and transitional. Cavitation is seen to significantly influence the evolution of pressure, boundary layer and loads on the cylinder surface. The cavitated shear layer rolls up into vortices, which are then shed from the cylinder, similar to a single-phase flow. However, the Strouhal number corresponding to vortex shedding decreases as the flow cavitates, and vorticity dilatation is found to play an important role in this reduction. At lower cavitation numbers, the entire vapour cavity detaches from the cylinder, leaving the wake cavitation-free for a small period of time. This low-frequency cavity detachment is found to occur due to a propagating condensation front and is discussed in detail. The effect of initial void fraction is assessed. The speed of sound in the free stream is altered as a result and the associated changes in the wake characteristics are discussed in detail. Finally, a large-eddy simulation of cavitating flow at $Re = 3900$ and $\sigma = 1.0$ is studied and a higher mean cavity length is obtained when compared to the cavitating flow at $Re = 200$ and $\sigma = 1.0$. The wake characteristics are compared to the single-phase results at the same Reynolds number and it is observed that cavitation suppresses turbulence in the near wake and delays three-dimensional breakdown of the vortices.

Key words: cavitation, vortex dynamics, wakes

1. Introduction

Cavitation is a phenomenon where liquid is abruptly converted into vapour when the pressure drops below the vapour pressure. Although cavitation on lifting bodies has been extensively studied both experimentally (e.g. Franc & Michel 1988; Arndt *et al.* 2000; Laberteaux & Ceccio 2001) and numerically (e.g. Kubota, Kato & Yamaguchi 1992; Coutier-Delgosha *et al.* 2007; Schnerr, Sezal & Schmidt 2008), relatively fewer studies exist for bluff bodies. Figure 1 shows the schematic of a

† Present address: 110 Union Street SE, 107 Akerman Hall, Minneapolis, MN 55455, USA.
Email address for correspondence: mahesh@aem.umn.edu

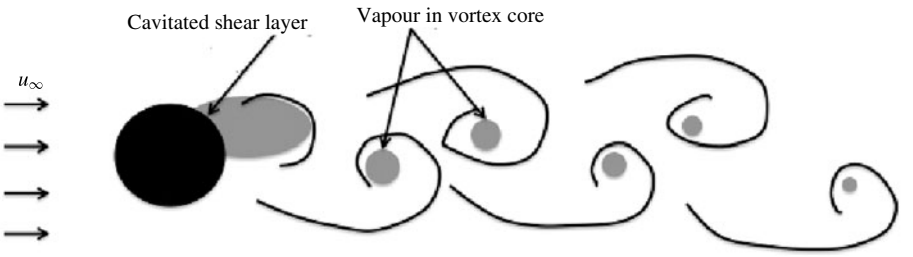

FIGURE 1. Schematic of vortex shedding and vapour formation in flow over a circular cylinder at low Reynolds number.

low-Reynolds-number cavitating flow over a cylinder. As the liquid accelerates past the bluff body, pressure drops in the shear layer, resulting in cavitation inception. The shear layer then rolls up into vortices and, depending on the conditions, the vortices can also cavitate. These vortices are shed from the body into the relatively high-pressure region in the wake. Here the vapour in the vortices collapses, resulting in pressure waves (also referred to as shock waves by many authors), which propagate both downstream and upstream. Cavitation behind bluff bodies can be categorized into three types (Fry 1984; Matsudaira, Gomi & Oba 1992): cyclic, fixed and transitional cavitation. A cyclic cavity sheds from the body periodically. A major portion of a fixed cavity remains attached to the body while small portions shed from the trailing edge of the attached portion. A transitional cavity displays both of these phenomena.

While bluff-body wakes have been studied extensively for single-phase flows (e.g. Roshko 1961; Bearman 1969; Williamson 1988, 1989; Hammache & Gharib 1991), only a few studies exist that shed light on the effect of cavitation on Kármán shedding and the near-wake characteristics. Varga & Sebestyen (1972) studied cavitation behind a circular cylinder with the main objective of understanding the noise generated by cavitation in water tunnels. Brandner *et al.* (2010) conducted experiments on a sphere and observed periodic shedding caused by re-entrant jets. A few other studies (e.g. Rao, Chandrasekhara & Seetharamiah 1972; Rao & Chandrasekhara 1976; Selim 1981) measured the shedding frequencies and cavity lengths in order to predict the effect of cavitation on the noise produced by a cavitating flow over a cylinder. Fry (1984) conducted detailed experiments on the flow past a cylinder to study the effect of free-stream velocity and cavitation number on the sound spectrum. He observed that the sound was correlated with the vortex shedding, and that larger cavities produced more sound upon collapse. Matsudaira *et al.* (1992) experimentally studied Kármán vortex cavities and found that regions of high impulse pressures occurred periodically behind the cylinder and were synchronized with the vortex shedding frequency. Balachandar & Ramamurthy (1999) studied the effect of cavitation on the base pressure coefficient and proposed a scaling based on wake parameters which unifies the wake pressure distribution for several cavitation numbers. Saito & Sato (2003) observed that cavities that collapse near solid walls generate high impact on the walls due to their proximity to the walls. They also observed three patterns of cavity collapse: three-dimensional (3D) radial, axial and two-dimensional (2D) radial. Seo, Moon & Shin (2008) used direct numerical simulation (DNS) to compute sound produced by a cavitating flow over a cylinder at $Re = 200$ and found that the main source of noise in the cavitating flow was the collapse of vapour cavities.

The wakes of 2D wedges are another canonical configuration that have been studied experimentally, and differ from cylinder wakes in some respects. Young &

Holl (1966) measured vortex shedding frequency behind 2D symmetric wedges and concluded that cavitation had a negligible effect on the frequency when the cavitation number was decreased from inception to half the incipient value. They also found that the shedding frequency reduced as choking conditions were approached. The flow over a wedge is relatively independent of Reynolds number unlike flow over circular cylinders. Also the dependence of the shedding frequency on cavitation number is different. Rao & Chandrasekhara (1976) observed that the vortex shedding frequency for cylinders increased to large values when choking conditions were approached. Also for symmetric wedges, the existence of a maximum in the variation of Strouhal number with cavitation number is well established (Young & Holl 1966; Belahadji, Franc & Michel 1995) unlike that for cylinders.

Another class of interesting flow in the field of separated cavitating flows is flow over axisymmetric nose-shaped objects. The fundamental difference in these objects from a cylinder is that there is a boundary layer reattachment which modulates the adverse pressure gradient experienced by the cavity closure. Arakeri & Acosta (1973) studied the effect of viscosity on cavitation inception on axisymmetric bodies and showed the presence of a laminar separation region upstream of the inception location. They also showed that the cavity became unstable and intermittent if the separation region was removed by tripping. Katz (1982, 1984) studied cavitation on axisymmetric bodies that underwent laminar separation and demonstrated that surface pressure fluctuations are independent of Reynolds numbers much like flow over a symmetric wedge. He also showed that, for a hemispherical body, the separation zone was smaller when compared to that of cylinders and that the inception region is located within the reattachment zone. Arakeri (1975) developed a semi-empirical approach to predict the location of cavity detachment over smooth bodies undergoing laminar separation and obtained good predictions for flow over a sphere, and so did Franc & Michel (1985) for circular and elliptical cylinders.

The objective of this paper is to study the effect of cavitation on the near-wake characteristics of a cylinder. We consider two Reynolds numbers and four different cavitation numbers. Two interesting phenomena are observed: a low-frequency cavity detachment; and a reduction in vortex shedding frequency with decreasing cavitation number. In single-phase flows, Gerrard (1966) characterized vortex shedding frequency using two important length scales: the vortex formation length, and the wake diffusion width. Strykowski & Sreenivasan (1990) showed that introduction of a strategically placed control cylinder resulted in an increased diffusion, causing vortex shedding suppression. They showed that vortex shedding frequency can be reduced and eventually completely suppressed. Mittal & Raghuvanshi (2001) and Dipankar, Sengupta & Talla (2007) performed numerical studies that confirmed the control cylinder experiments. In this study, we analyse the effect of cavitation in reducing the vortex shedding frequency.

Also, the effect of cavitation nuclei which are included in the simulations in the form of initial vapour volume fraction is studied. Cavitation nuclei are known to play an important role in the inception process (Katz 1984; Arndt & Maines 2000; Arndt 2002; Hsiao & Chahine 2005). Within the context of homogeneous mixture models, the initial vapour volume fraction determines the speed of sound which is very sensitive to vapour volume fraction values <0.1. The dynamics of pressure waves may therefore be affected even in advanced stages of cavitation.

The Reynolds numbers considered in this study are 200 and 3900, which are low enough to allow parametric studies. It should be noted that these Reynolds numbers are low for any experimental measurement to be possible. A circular cylinder is

chosen as the bluff body, since the Kármán shedding behind a cylinder is well understood for single-phase flows. The paper is organized as follows. Section 2 explains the physical model used for cavitation, along with the governing equations for the compressible mixture of water and water vapour. This section also describes the predictor–corrector algorithm (Gnanaskandan & Mahesh 2014, 2015) used to solve the governing equations. Section 3 validates the numerical algorithm for flow over a hemispherical nose-shaped body. Section 4 describes the problem and outlines details of the computational grid and boundary conditions. Section 5 discusses the effect of cavitation number and the mechanism of reduction of vortex shedding frequency. In § 6, the effect of initial void fraction is discussed in detail. A large-eddy simulation (LES) of turbulent ($Re = 3900$) flow over a cylinder is presented in § 7 and a summary in § 8 concludes the paper.

2. Governing equations and numerical method

Cavitation inception studies are often performed using the discrete Lagrangian approach, while developed cavitation simulations have traditionally preferred a continuum approach. The most commonly used physical model within the continuum approach is the homogeneous mixture model (e.g. Kunz *et al.* 2000; Senocak & Shyy 2002; Singhal *et al.* 2002; Shin, Iwata & Ikohagi 2003; Schmidt, Schnerr & Thalhamer 2009; Gnanaskandan & Mahesh 2015), which is used in the current simulations. The homogeneous mixture model assumes the mixture of constituent phases to be a single compressible fluid and the phases to be in thermal and mechanical equilibrium. Surface tension effects are assumed small and are neglected.

Although the homogeneous mixture approach is the most commonly used physical model to predict developed cavitation, there are some potential limitations with this model particularly pertaining to cavitation inception. Cavitation inception in homogeneous models depends only on the difference between local pressure and vapour pressure. However, other factors that influence inception such as non-condensible gases, size of nuclei and their distribution are not accounted for in this study. Further, discrete bubble dynamics on a scale smaller than the computational mesh are not represented. Overall, however, the dynamics of cavitation after inception are captured well by this model, as reflected in our simulations of flow over a hydrofoil and wedge (Gnanaskandan & Mahesh 2015) and in the validation case presented in § 3 of this paper.

The governing equations are the compressible Navier–Stokes equation for the mixture of liquid and vapour, along with a transport equation for vapour. The governing equations are Favre-averaged and then spatially filtered to perform LES. A dynamic Smagorinsky model is used for the subgrid terms. The unfiltered governing equations are

$$\left.\begin{aligned} \frac{\partial \rho}{\partial t} &= -\frac{\partial}{\partial x_k}(\rho u_k), \\ \frac{\partial \rho u_i}{\partial t} &= -\frac{\partial}{\partial x_k}(\rho u_i u_k + p\delta_{ik} - \sigma_{ik}), \\ \frac{\partial \rho e_s}{\partial t} &= -\frac{\partial}{\partial x_k}(\rho e_s u_k - Q_k) - p\frac{\partial u_k}{\partial x_k} + \sigma_{ik}\frac{\partial u_i}{\partial x_k}, \\ \frac{\partial \rho Y}{\partial t} &= -\frac{\partial}{\partial x_k}(\rho Y u_k) + S_e - S_c, \end{aligned}\right\} \tag{2.1}$$

where ρ, u_i, e_s and p are the density, velocity, internal energy and pressure, respectively, of the mixture and Y is the vapour mass fraction. The mixture density is

$$\rho = \rho_l(1-\alpha) + \rho_g\alpha, \tag{2.2}$$

where ρ_l is the density of liquid, ρ_g is the density of vapour and α is the vapour volume fraction, which is related to the vapour mass fraction by

$$\rho_l(1-\alpha) = \rho(1-Y) \quad \text{and} \quad \rho_g\alpha = \rho Y. \tag{2.3a,b}$$

The system is closed using a mixture equation of state (Gnanaskandan & Mahesh 2015):

$$p = Y\rho R_g T + (1-Y)\rho K_l T\frac{p}{p+P_c}. \tag{2.4}$$

Here, $R_g = 461.6$ J kg^{-1} K^{-1}, $K_l = 2684.075$ J kg^{-1} K^{-1} and $P_c = 786.333 \times 10^6$ Pa are constants associated with the equation of state of vapour and liquid. The stiffened equation of state is used for water and the ideal gas equation of state for vapour. The stiffened equation of state has a form very similar to the ideal gas equation of state. It is suitable for liquids with non-isentropic changes and is hence chosen in this study. The expression for e_s is given by

$$\rho e_s = \rho C_{vm} T + \rho(1-Y)\frac{P_c K_l T}{p+P_c}, \tag{2.5}$$

where $C_{vm} = (1-Y)C_{vl} + YC_{vg}$ and C_{vl} and C_{vg} are the specific heats at constant volume for liquid and vapour, respectively. The viscous stress σ_{ij} and heat flux Q_i are given by

$$\sigma_{ij} = \mu\left(\frac{\partial u_i}{\partial x_j} + \frac{\partial u_j}{\partial x_i} - \frac{2}{3}\frac{\partial u_k}{\partial x_k}\delta_{ij}\right) \quad \text{and} \quad Q_i = k\frac{\partial T}{\partial x_i}, \tag{2.6a,b}$$

where μ and k are the mixture viscosity and mixture thermal conductivity, respectively. In addition, S_e and S_c are source terms for evaporation of water and condensation of vapour and are given by

$$\left.\begin{aligned} S_e &= C_e\alpha^2(1-\alpha)^2\frac{\rho_l}{\rho_g}\frac{\max(p_v-p,0)}{\sqrt{2\pi R_g T}}, \\ S_c &= C_c\alpha^2(1-\alpha)^2\frac{\max(p-p_v,0)}{\sqrt{2\pi R_g T}}, \end{aligned}\right\} \tag{2.7}$$

where p_v is the vapour pressure, and C_e and C_c are empirical constants whose value is 0.1 (Saito *et al.* 2007). Vapour pressure is related to temperature by

$$p_v = p_k \exp\left[\left(1-\frac{T_k}{T}\right)(a+(b-cT)(T-d)^2)\right], \tag{2.8}$$

where $p_k = 22.130$ MPa, $T_k = 647.31$ K, $a = 7.21$, $b = 1.152 \times 10^{-5}$, $c = -4.787 \times 10^{-9}$ and $d = 483.16$.

The simulations use the algorithm developed by Gnanaskandan & Mahesh (2015) to simulate cavitating flows on unstructured grids. The algorithm makes use of a

novel predictor–corrector approach. In the predictor step, the governing equations are discretized using a symmetric non-dissipative scheme, where the fluxes at a cell face are given by

$$\phi_{f_c} = \frac{\phi_{icv1} + \phi_{icv2}}{2} + \frac{1}{2}(\nabla\phi|_{icv1} \cdot \Delta\boldsymbol{x}^{icv1} + \nabla\phi|_{icv2} \cdot \Delta\boldsymbol{x}^{icv2}), \tag{2.9}$$

where $\Delta\boldsymbol{x}^{icv1} = \boldsymbol{x}_{f_c} - \boldsymbol{x}_{icv1}$, and $\nabla\phi|_{icv1}$ denotes the gradient defined at $icv1$, which is computed using a least-squares method. The viscous fluxes are split into compressible and incompressible contributions and treated separately. Once the fluxes are obtained, a predicted value $\widehat{q}_j^{n+1}$ is computed using an explicit Adams–Bashforth scheme:

$$\widehat{q}_j^{n+1} = \widehat{q}_j^{n} + \frac{\Delta t}{2}[3\,\mathrm{RHS}_j(\widehat{\boldsymbol{q}}^n) - \mathrm{RHS}_j(\widehat{\boldsymbol{q}}^{n-1})], \tag{2.10}$$

where RHS_j denotes the jth component of the right-hand side of the governing equations, and the superscript n denotes the nth time step. The final solution q_j^{n+1} at $t + \Delta t$ is obtained from a corrector scheme

$$q_{j,cv}^{n+1} = \widehat{q}_{j,cv}^{n+1} - \frac{\Delta t}{V_{cv}} \sum_{faces} (F_f^* n_f) A_f, \tag{2.11}$$

where F_f^* is the filter numerical flux of the following form:

$$F_{fc}^* = \tfrac{1}{2} R_{fc} \Phi_{fc}^*. \tag{2.12}$$

Here R_{fc} is the right eigenvector at the face computed using the Roe average of the variables from left and right control volumes. The expression for the lth component of Φ^*, ϕ^{*l}, is given by

$$\phi_{fc}^{*l} = k\theta_{fc}^l \phi_{fc}^l, \tag{2.13}$$

where k is an adjustable parameter and θ_{fc} is Harten's switch function, given by

$$\theta_{fc} = \sqrt{0.5(\widehat{\theta}_{icv1}^2 + \widehat{\theta}_{icv2}^2)}, \quad \widehat{\theta}_{icv1} = \frac{|\beta_{fc}| - |\beta_{f1}|}{|\beta_{fc}| + |\beta_{f1}|}, \quad \widehat{\theta}_{icv2} = \frac{|\beta_{f2}| - |\beta_{fc}|}{|\beta_{f2}| + |\beta_{fc}|}. \tag{2.14a–c}$$

Here, $\beta_f = R_f^{-1}(q_{icv2} - q_{icv1})$ is the difference between characteristic variables across the face. For ϕ^ℓ, the Harten–Yee total variation diminishing (TVD) form is used as suggested by Yee, Sandham & Djomehri (1999):

$$\left.\begin{aligned} \phi_{f_c}^\ell &= \tfrac{1}{2}\Psi(a_{f_c}^\ell)(g_{icv1}^\ell + g_{icv2}^\ell) - \Psi(a_{f_c}^\ell + \gamma_{f_c}^\ell)\beta_{f_c}^\ell, \\ \gamma_{f_c}^\ell &= \frac{1}{2}\frac{\Psi(a_{f_c}^\ell)(g_{icv2}^\ell - g_{icv1}^\ell)\beta_{f_c}^\ell}{(\beta_{f_c}^\ell)^2 + \epsilon}, \end{aligned}\right\} \tag{2.15}$$

where $\epsilon = 10^{-7}$, $\Psi(z) = \sqrt{\delta + z^2}$ $(\delta = 1/16)$ is introduced for entropy fixing and $a_{f_c}^\ell$ is an element of the Jacobian matrix. Park & Mahesh (2007) and Gnanaskandan & Mahesh (2015) proposed a modification to Harten's switch to accurately represent under-resolved turbulence for single-phase and multiphase flow mixtures, respectively, by multiplying θ_{f_c} by $\theta_{f_c}^\star$ given by

$$\left.\begin{aligned} \theta_{f_c}^\star &= \tfrac{1}{2}(\theta_{icv1}^\star + \theta_{icv2}^\star) + |(\alpha_{icv2} - \alpha_{icv1})|, \\ \theta_{icv1}^\star &= \frac{(\boldsymbol{\nabla}\cdot\boldsymbol{u})_{icv1}^2}{(\boldsymbol{\nabla}\cdot\boldsymbol{u})_{icv1}^2 + \Omega_{icv1}^2 + \epsilon}. \end{aligned}\right\} \tag{2.16}$$

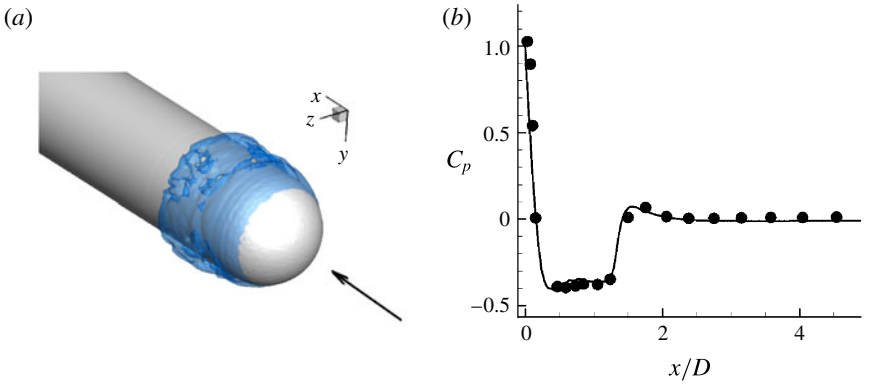

FIGURE 2. (Colour online) (*a*) Instantaneous isocontour ($\alpha = 0.1$) of void fraction, and (*b*) time-averaged C_p distribution (——, LES; ●, experiment of Rouse & McNown (1948)).

Gnanaskandan & Mahesh (2015) have evaluated this algorithm for a variety of flows, including a cavitating shock tube and turbulent cavitating flow over a hydrofoil and a wedge.

3. Validation: cavitation over a hemispherical nose-shaped body

We consider partial cavitation over a hemispherical nose-shaped bluff body for validation. We compare our LES results to the experimental results of Rouse & McNown (1948). The diameter of the hemisphere is D and the length of the cylindrical body is $50D$. The extent of the domain is $50D$ in all directions. The Reynolds number based on the diameter of the hemisphere and free-stream velocity is $Re_D = 1.36 \times 10^5$ and the cavitation number is 0.4. The grid spacing used is $0.002D$ in both streamwise and wall-normal directions and the grid is clustered close to the cavity inception region. A uniform grid spacing of $0.01D$ is used in the circumferential direction. The solution is initialized with a void fraction of $\alpha_0 = 0.01$. The non-dimensional time step $tu_\infty/D = 2 \times 10^{-5}$ and the solution is advanced in a time-accurate manner. Figure 2(*a*) shows instantaneous isocontours of void fraction which vary in the circumferential direction and are unsteady in time. Figure 2(*b*) compares the time-averaged C_p distribution to the experimental data (Rouse & McNown 1948); good agreement is obtained, indicating the suitability of the method in predicting bluff-body cavitation also.

4. Problem description

Figure 3 shows a schematic of the problem. A circular cylinder of diameter D is placed at the centre of a circular domain of radius equal to $100D$, chosen to minimize acoustic reflection from the far-field boundaries. The free-stream flow is spatially uniform and the velocity is in the positive x direction as shown in figure 3. The subscript ∞ is used to denote free-stream conditions and ρ_∞, p_∞, u_∞ and μ_∞ denote free-stream density, pressure, velocity and dynamic viscosity, respectively. Free-stream conditions are imposed on all far-field boundaries. Acoustically absorbing boundary conditions (Colonius 2004) are applied in the sponge layer shown in figure 3. The term $-\gamma(\boldsymbol{q} - \boldsymbol{q}_{ref})$ is added to the governing equations, where γ is zero outside the sponge layer, $\boldsymbol{q}$ denotes the vector of conservative variables and the

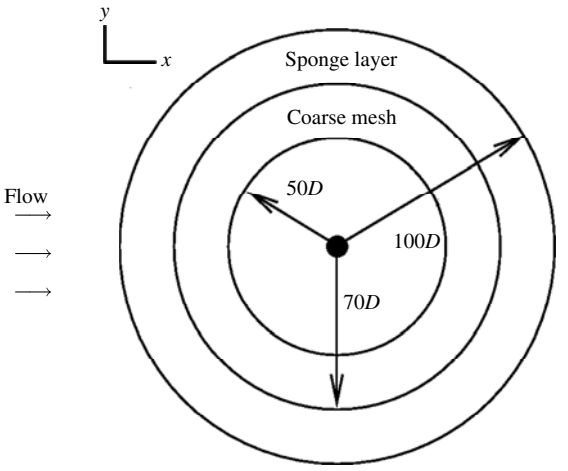

FIGURE 3. Computational domain illustrating sponge layer and region of coarse mesh (not to scale).

Reynolds number (Re)	Cavitation number (σ)	Initial void fraction (α_0)
200	2.0	0.01
200	1.0	0.01
200	0.7	0.01
200	0.5	0.01
200	1.0	0.005
3900	1.0	0.01

TABLE 1. Flow conditions used in the simulations.

subscript '*ref*' denotes the reference solution to which the flow inside the sponge layer is damped, which in this case is the free-stream value. Also the mesh is made coarse in the far field to further reduce any reflections.

Table 1 lists the flow conditions for all the cases considered in this study. Here, cavitation number $\sigma = (p_\infty - p_v)/(0.5\rho_\infty u_\infty^2)$ and the Reynolds number is given by $Re = (\rho_\infty u_\infty D)/\mu_\infty$. The simulations are initialized with a spatially uniform void fraction (α_0) that nucleates the cavitation. Insensitivity to computational grid and domain size is demonstrated using two grids and two domain sizes for one case ($Re = 200$ and $\sigma = 1.0$). The mesh spacing for the fine grid is $0.005D \times 0.01D$ in the radial and azimuthal directions near the wall and stretches to $0.03D \times 0.03D$ at approximately $2D$ downstream and then further stretches to $0.07D \times 0.07D$ at a distance of $5D$ downstream. The coarse grid has a near-wall mesh spacing of $0.01D \times 0.02D$ and stretches to $0.05D \times 0.05D$ at approximately $2D$ downstream. The corresponding domain radii are $100D$ and $50D$, respectively.

Figure 4 shows the lift and drag coefficients as functions of time for both the grids. Figure 5 shows the comparison of the mean and fluctuation of void fraction between the two grids. Note that the solutions show good agreement, and the fine grid and the larger domain have therefore been used for all the subsequent simulations at $Re = 200$. The mesh spacing and the spanwise extent for the 3D simulation are the same as that

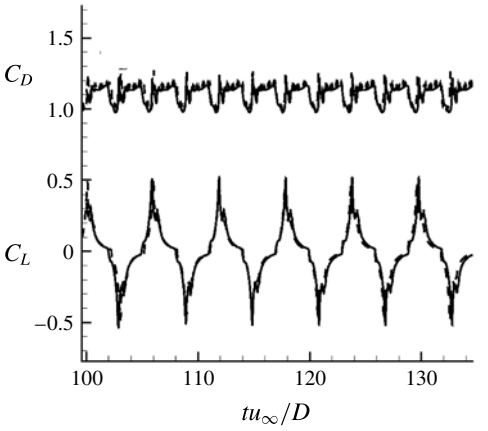

FIGURE 4. Comparison of lift and drag coefficient history showing grid convergence between two grids and domain insensitivity between two domains: – – – –, coarse grid, small domain; ——, fine grid, big domain.

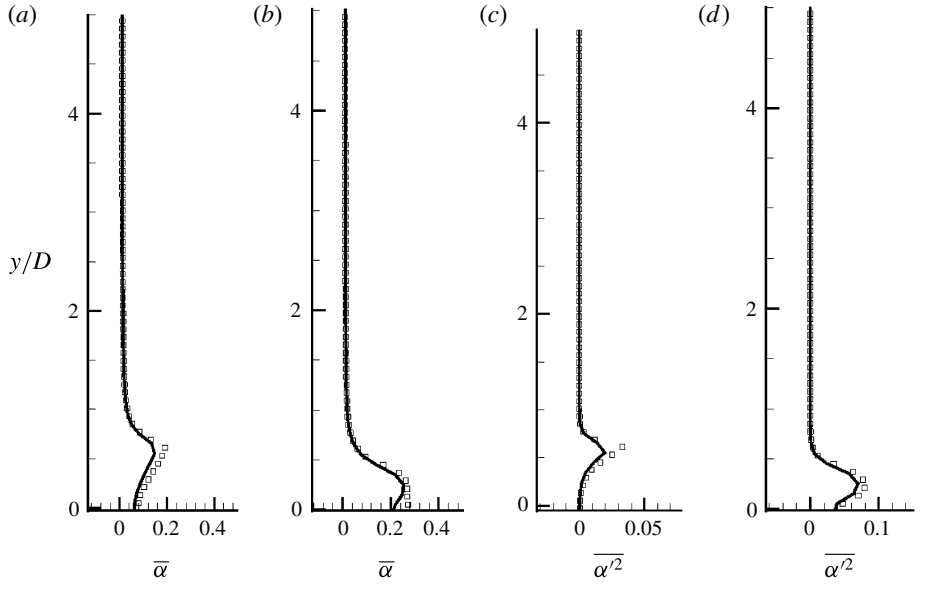

FIGURE 5. Comparison of (*a*,*b*) mean void fraction and (*c*,*d*) fluctuation in void fraction, for (*a*,*c*) $x/D = 0.6$ and (*b*,*d*) $x/D = 2.0$: ——, fine grid, big domain; □, coarse grid, small domain.

in the simulation of Verma & Mahesh (2012) for a single-phase flow at the same Reynolds number, where good agreement was obtained with experiment. The near-wall mesh spacing is $0.002D \times 0.005D$ in size and stretches to $0.004D \times 0.008D$ at a downstream location of $5D$. A total of 80 points are used in the spanwise direction. Since the presence of vapour decreases the effective Reynolds number, this resolution is deemed sufficient.

The nature of the instantaneous solution is illustrated in figure 6(*a*) using the $Re = 200$ and $\sigma = 1.0$ simulation. The void fraction contours show the presence

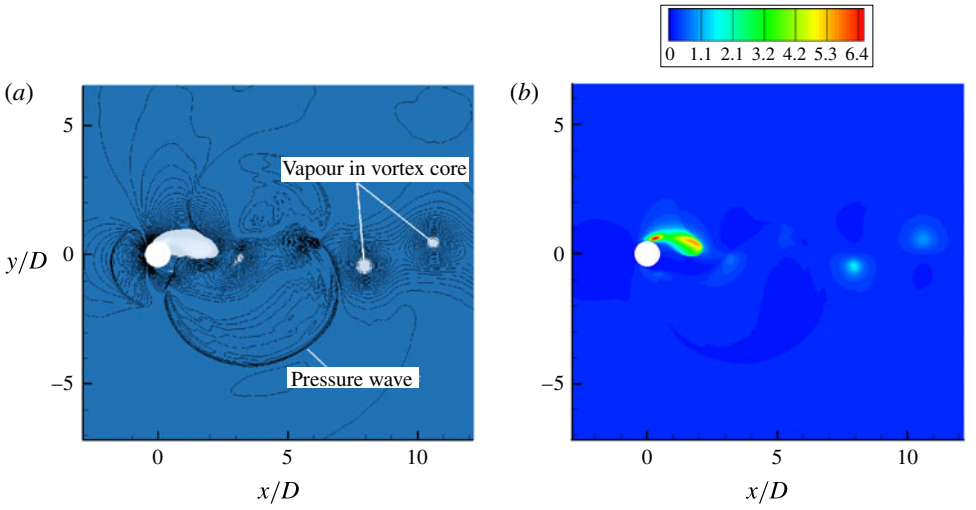

FIGURE 6. (Colour online) (*a*) Instantaneous snapshot showing coloured contours of void fraction and contour lines showing pressure. (*b*) Instantaneous Mach-number contour.

of vapour immediately downstream of the cylinder as well as in the core of the Kármán vortices downstream. The superposed contour lines of pressure show the presence of 'pressure waves', which are compression waves that form when vapour pockets collapse in the higher-pressure regions downstream of the cylinder. The speed of sound drops significantly in regions of vapour, resulting in supersonic Mach numbers in some parts of the flow. Figure 6(*b*) reveals Mach numbers as high as 6 in the cavitated shear layer immediately downstream of the cylinder. The large spatial variation in sound speed results in the pressure waves refracting through the near-field vapour and impinging upon the cylinder. The $Re = 3900$ flow exhibits similar qualitative behaviour and is discussed in § 7.

The effect of σ on the time-averaged flow behind the cylinder as well as the unsteady loads on the cylinder are discussed below (§ 5) for $Re = 200$. The $\sigma = 0.7$ and 0.5 flows exhibit a 'low-frequency cavity detachment' phenomenon, where a pocket of vapour attached to the cylinder sheds downstream. This behaviour is analysed in § 5.6. The σ value also affects the Kármán vortex shedding frequency, which is discussed in § 5.7. The influence of α_0 is considered in § 6, and LES of the $Re = 3900$ flow is discussed in § 7.

5. Effect of cavitation number (σ)

Cavitating flows at three different cavitation numbers ($\sigma = 1.0$, 0.7 and 0.5) are considered and compared to the non-cavitating flow at $\sigma = 2.0$. The cavitation number is varied by changing the free-stream velocity while keeping all other quantities constant. The flow is seeded with a free-stream void fraction of $\alpha_0 = 0.01$.

5.1. *Pressure on the cylinder surface*

Figure 7(*a*) shows the mean pressure coefficient on the cylinder surface. Here, $\theta = 0°$ and 180° correspond to the leading-edge stagnation point and trailing edge, respectively. In the absence of cavitation, the pressure coefficient decreases to its

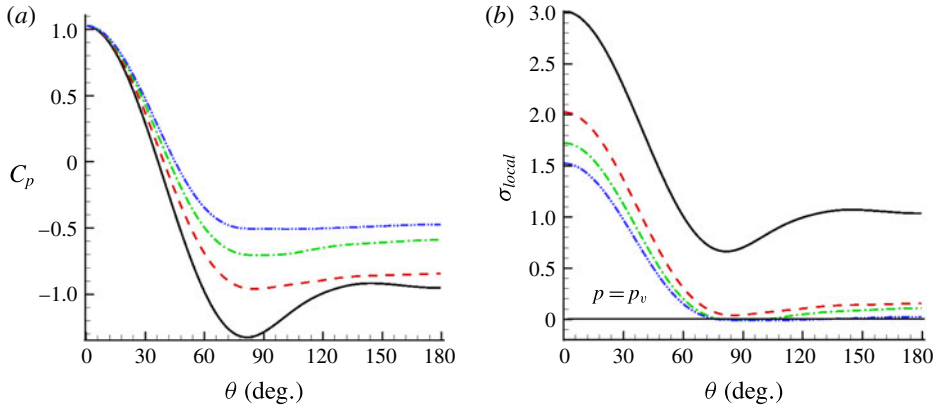

FIGURE 7. (Colour online) (*a*) Time-averaged C_p on the cylinder, and (*b*) time-averaged distribution of σ_{local} on the cylinder: ——, $\sigma = 2.0$; – – – –, $\sigma = 1.0$; –·–·–, $\sigma = 0.7$; — · · —, $\sigma = 0.5$.

minimum value at approximately 80° as the flow accelerates from the stagnation point, then increases as the flow decelerates, prior to becoming approximately constant in the wake region at the trailing edge. Cavitation is seen to decrease the magnitude of minimum C_p, with lower values of σ causing a larger decrease in magnitude. This is because, once flow cavitates (close to the minimum C_p location), the pressure in the vapour region remains close to the vapour pressure; it does not further decrease with fluid acceleration. The upstream flow therefore sees lower values of favourable pressure gradient and the downstream flow experiences approximately constant pressure.

Defining $\sigma_{local} = 2(p - p_v)/\rho_\infty u_\infty^2$ and $\sigma_\infty = 2(p_\infty - p_v)/\rho_\infty u_\infty^2$ yields $\sigma_{local} = C_p + \sigma_\infty$. Figure 7(*b*) reveals small values for σ_{local} downstream of the minimum C_p location on the cylinder surface for the cavitating flows. Also, for $\sigma = 1.0$ the mean pressure is always above the vapour pressure, whereas for $\sigma = 0.7$ and 0.5, the mean pressure falls below the vapour pressure and recovers to values slightly above the vapour pressure near the trailing edge of the cylinder. High-density fluid can therefore be present near the trailing edge, in the mean flow. This behaviour is illustrated in figure 8, which shows contours of instantaneous and mean void fraction. Since, when $\sigma = 1.0$, only the instantaneous pressure falls below the vapour pressure, vapour is observed largely in the core of the Kármán vortices. In contrast, when $\sigma = 0.7$ and 0.5, since the mean pressure in the near wake is also below the vapour pressure, vapour is also present in substantial portions of the near wake. Figure 9 shows the variation of mean void fraction and mixture density along the cylinder surface from the leading edge towards the trailing edge. Note the presence of higher-density fluid near the trailing edge, and that the mean void fraction is not necessarily 1 due to vapour unsteadiness. Although vapour decreases the density of the mixture, the density is still skewed towards the liquid due to its significantly higher value.

5.2. *Velocity divergence due to cavitation*

Cavitation causes density change, which implies a considerable change in the divergence of the velocity field. Figure 10 shows the mean velocity divergence ($\nabla \cdot \boldsymbol{V}$) contours for all the cavitating cases. Expansion caused due to cavitation

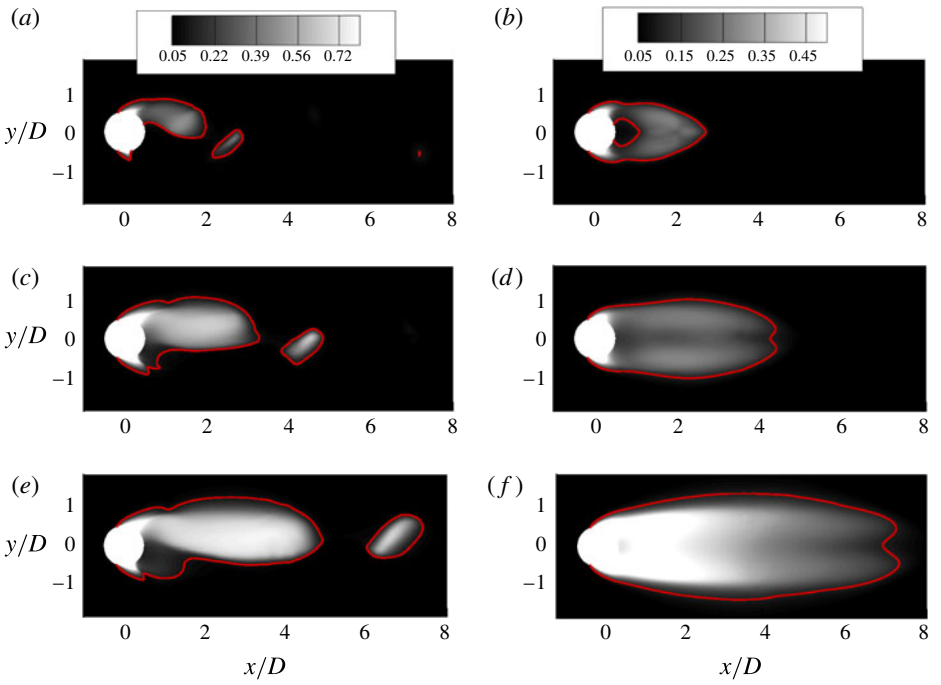

FIGURE 8. (Colour online) Instantaneous (*a*,*c*,*e*) and mean (*b*,*d*,*f*) void fraction contours for (*a*,*b*) $\sigma = 1.0$, (*c*,*d*) $\sigma = 0.7$ and (*e*,*f*) $\sigma = 0.5$.

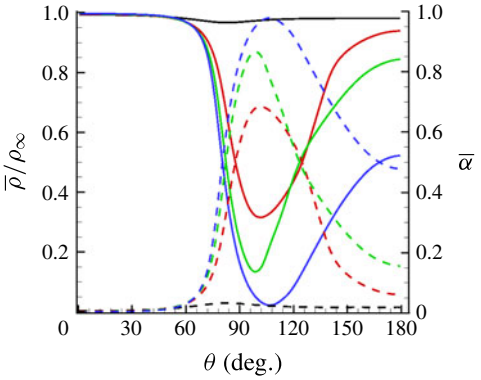

FIGURE 9. (Colour online) Variation of density (solid) and void fraction (dashed) along the cylinder surface as a function of azimuthal location: $\sigma = 2.0$ (black), $\sigma = 1.0$ (red), $\sigma = 0.7$ (green), $\sigma = 0.5$ (blue).

can be seen as positive divergence and, as the flow cavitates more, the region of positive $\nabla \cdot \boldsymbol{V}$ also increases due to the increased amount of vapour. It is interesting to note a compression region (negative $\nabla \cdot \boldsymbol{V}$) downstream of the expansion region, and the magnitude of this compression region appears to decrease as the cavitation number reduces. This behaviour can be understood by revisiting the mean void fraction contours in figure 8. For $\sigma = 1.0$, there is a large decrease in void fraction corresponding to the region of negative divergence. This is a result of the cavitating

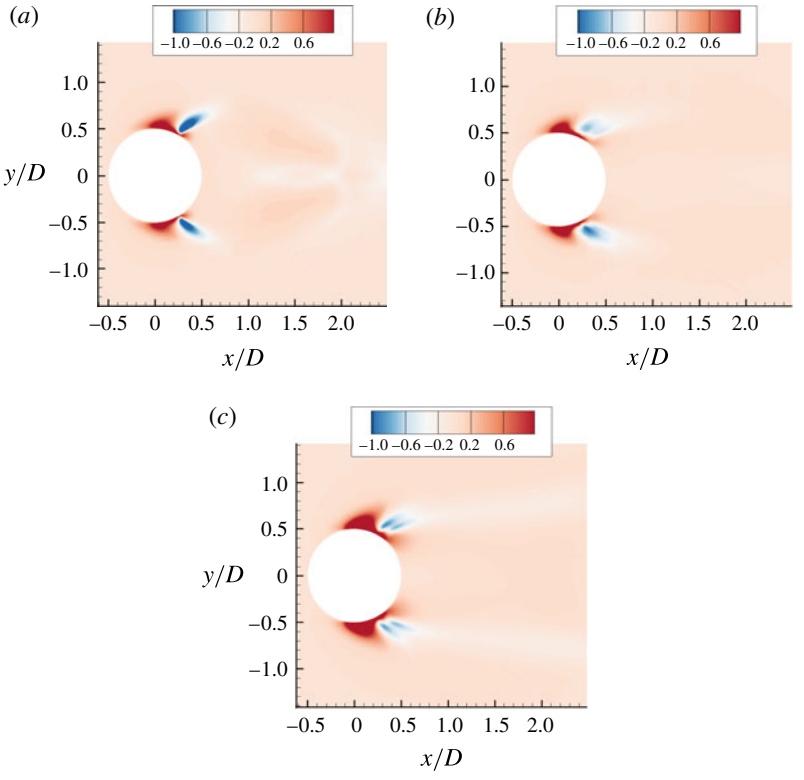

FIGURE 10. (Colour online) Contours of divergence of velocity field for (*a*) $\sigma = 1.0$, (*b*) $\sigma = 0.7$ and (*c*) $\sigma = 0.5$.

vortex being shed from the body, which takes away vapour from close to the body, leading to a sharp decrease in void fraction in the mean. However, we observe that, for $\sigma = 0.7$ and 0.5, the void fraction does not decrease as much as in $\sigma = 1.0$, since for these cases the cavitating vortex sheds from the attached cavity at a downstream location. Thus this compression region is an indication of some amount of vapour being converted back to water.

5.3. *Boundary layer on the cylinder surface*

The pressure along the cylinder surface affects the evolution of the boundary layer. Figure 11 shows boundary layer velocity profiles at four different azimuthal locations for $\sigma = 2.0$ and 0.5. Mean values are shown on top and root mean square values on the bottom. The azimuthal locations $\theta = 70°$, $90°$, $110°$ and $130°$ are chosen to represent regions of favourable pressure gradient, minimum pressure, adverse pressure gradient and separated flow, respectively. Figure 11 contrasts only $\sigma = 2.0$ (non-cavitating) and 0.5 (cavitating) cases for clarity. Here, u_θ is the tangential velocity and r is the normal distance from the cylinder at any given azimuthal location. Cavitation causes expansion (positive dilatation) at the inception location, which causes the flow upstream to decelerate as seen in figure 11. For instance, the maximum velocity in the boundary layer ($u_{\theta_{max}}/u_\infty$) drops to a value of 1.10 for $\sigma = 0.5$ from a value of 1.34 for $\sigma = 2.0$ at an azimuthal location of 70°. The

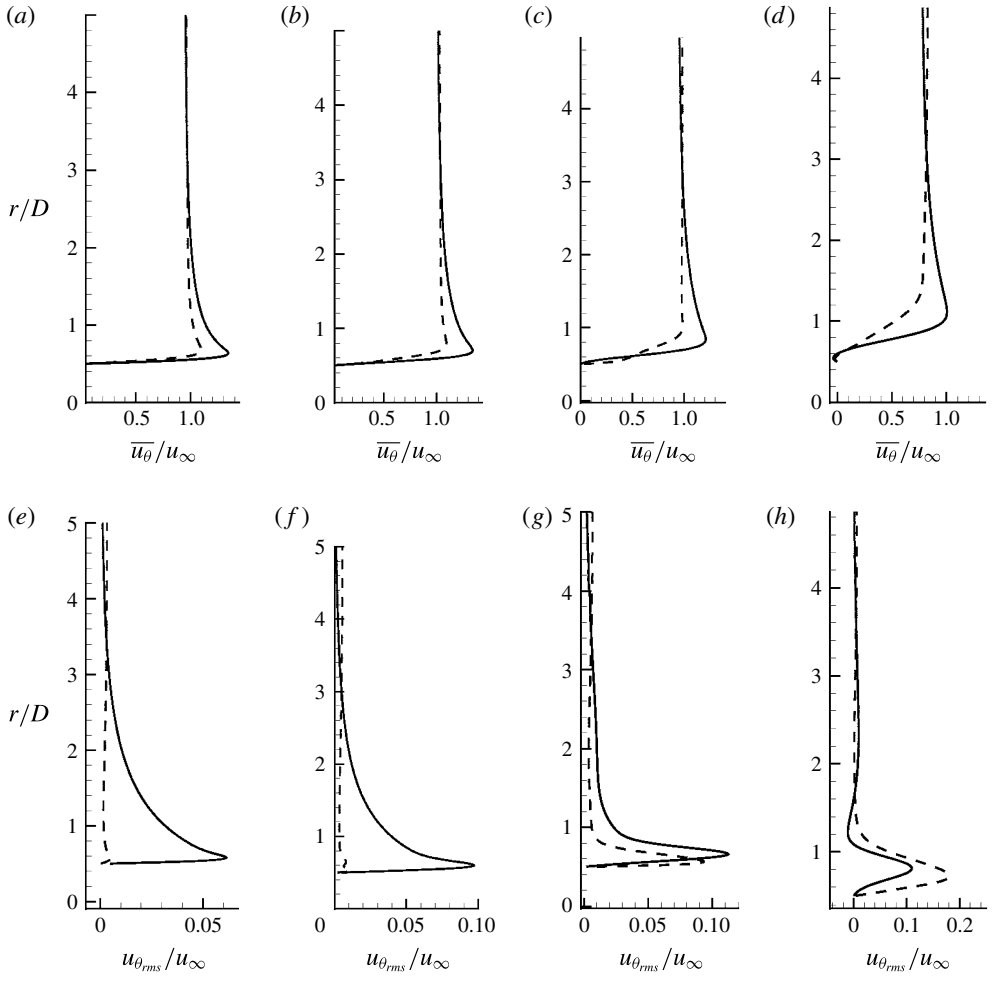

FIGURE 11. Mean (*a–d*) and root mean square (*e–h*) boundary layer profiles at four azimuthal locations $\theta = 70°$ (*a*,*e*), 90° (*b*,*f*), 110° (*c*,*g*) and 130° (*d*,*h*): ——, $\sigma = 2.0$; and – – – –, $\sigma = 0.5$.

fluctuation levels of the cavitating flow are much lower at the first two locations, indicating that the flow becomes steady due to cavitation. The location where maximum velocity in the boundary layer occurs is also shifted away from the wall for the cavitating flow as a result. The magnitude of the maximum velocity in the boundary layer ($u_{\theta_{max}}$) and the location of its occurrence are plotted as a function of θ in figure 12 for all four cases. Note that the boundary layer thickens with decreasing cavitation number. Also the magnitude of $u_{\theta_{max}}$ initially increases in the favourable pressure gradient region and then drops after 80°. The drop in magnitude of $u_{\theta_{max}}$ is rapid for $\sigma = 2.0$ after 90° when compared to the cavitating flow, which points to a rapid thickening of the boundary layer leading to separation. The location of maximum velocity is shifted away from the wall as the flow cavitates more, and this difference between cavitating and non-cavitating flow increases further as we move closer to the trailing edge.

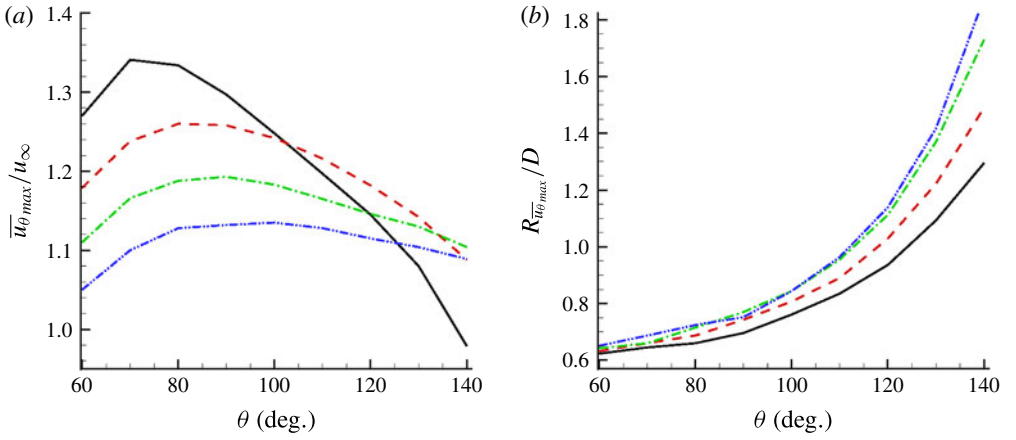

FIGURE 12. (Colour online) (*a*) Variation of maximum velocity in the boundary layer as a function of azimuthal location, and (*b*) variation of location of maximum velocity in the boundary layer as a function of azimuthal location: ——, $\sigma = 2.0$; – – – –, $\sigma = 1.0$; –·–·–, $\sigma = 0.7$; — · · —, $\sigma = 0.5$.

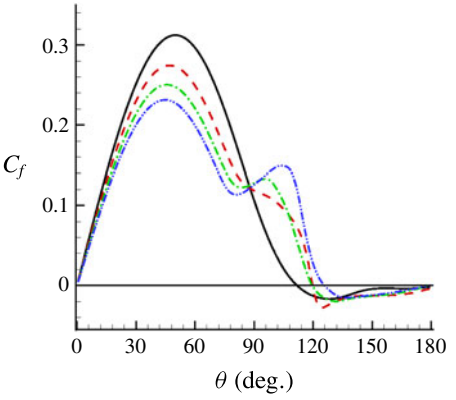

FIGURE 13. (Colour online) Time-averaged skin friction coefficient distribution on the cylinder: ——, $\sigma = 2.0$: – – – –, $\sigma = 1.0$; –·–·–, $\sigma = 0.7$; — · · —, $\sigma = 0.5$.

Figure 13 shows the time-averaged skin friction distribution along the cylinder. The magnitude of C_f initially increases in the favourable pressure gradient region and then drops as the boundary layer thickens due to adverse pressure gradient. Note that the cavitating flows have a reduced skin friction value compared to $\sigma = 2.0$ up to 80° due to the deceleration caused by the vapour cavity. Flow expansion due to cavitation also causes the flow downstream of the inception location to accelerate. This can be seen in the form of a local increase in skin friction coefficient in figure 13 for $\sigma = 1.0$, 0.7 and 0.5 at approximately 80°. The flow separates under the influence of adverse pressure gradient at approximately 110° for $\sigma = 2.0$. The separation location for the cavitated flows, however, shifts downstream to approximately 120° for $\sigma = 1.0$ and 0.7 and to approximately 125° for $\sigma = 0.5$. This behaviour is in contrast to the observations of Arakeri (1975) and Ramamurthy & Bhaskaran (1977), who found that the separation point moves upstream as the flow cavitates more. The main reason for

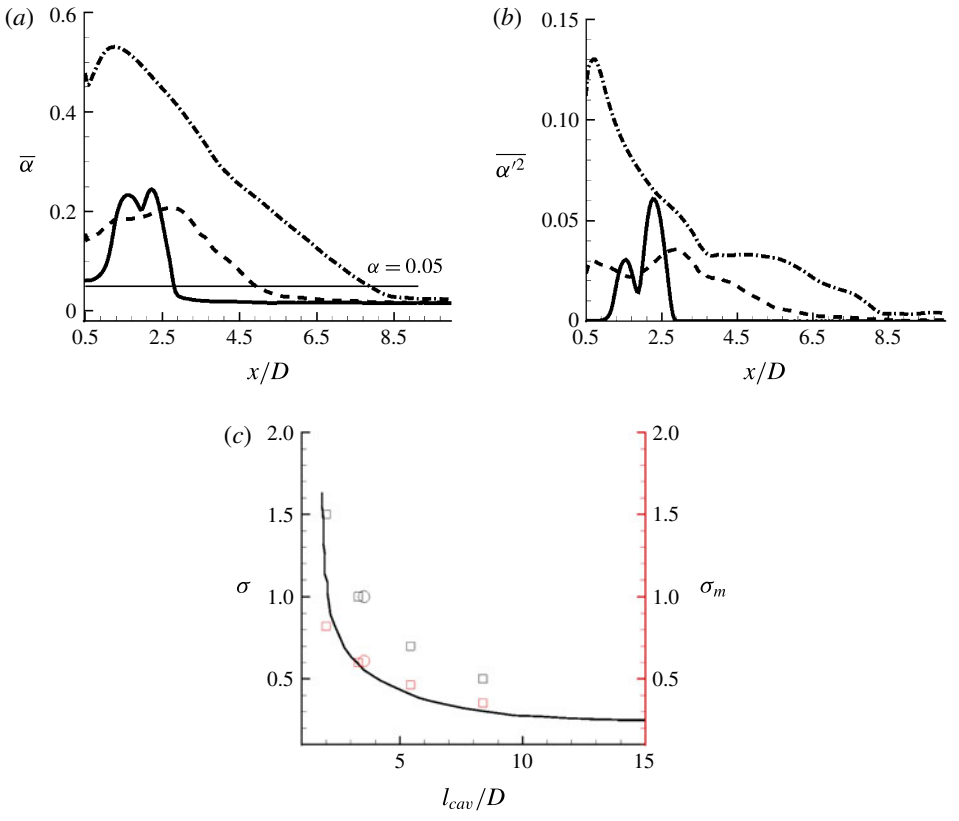

FIGURE 14. (Colour online) Variation of (*a*) $\overline{\alpha}$ and (*b*) $\overline{\alpha'^2}$ with downstream distance in the wake: ——, $\sigma = 1.0$; – – –, $\sigma = 0.7$; –·–·–, $\sigma = 0.5$. (*c*) Variation of normalized cavity length with cavitation number: ——, experimental fit (Rao & Chandrasekhara 1976); □, $Re = 200$; ○, $Re = 3900$.

this discrepancy is the fact that the homogeneous mixture model predicts that the inception point is upstream of the separation point. The cavitation criterion in the model is simply based on the difference between the local pressure and the vapour pressure, and hence cavitation occurs as soon as the pressure drops below the vapour pressure (although there is a finite rate at which vapour is produced). However, in reality, cavitation does not occur immediately at the location where the pressure drops below the vapour pressure, but occurs downstream of the separation point. In the numerical simulations, with the separation point downstream of the inception point, the acceleration induced by expansion pushes the separation point further downstream as the flow cavitates more. In contrast, in the experiments of Arakeri (1975) and Ramamurthy & Bhaskaran (1977), the separation point is ahead of the inception point and the cavitation-induced expansion causes flow deceleration upstream leading to an earlier separation.

5.4. *Cavity length*

The mean cavity length increases progressively as the cavitation number decreases. The mean length of the cavity is computed from figure 14(*a*) as the location

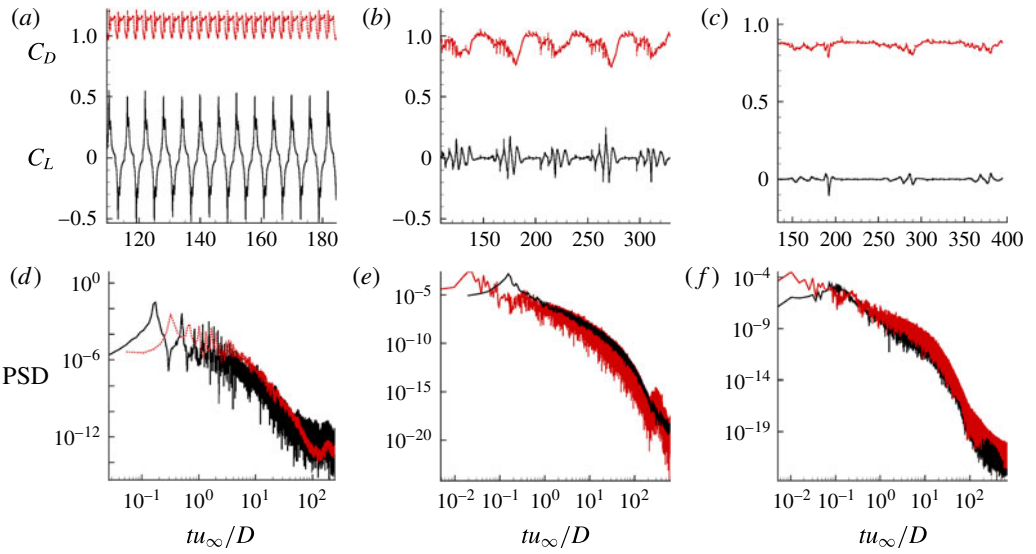

FIGURE 15. (Colour online) Lift and drag history (*a–c*) and their spectra (*d–f*) for (*a,d*) $\sigma = 1.0$, (*b,e*) $\sigma = 0.7$ and (*c,f*) $\sigma = 0.5$: ——, C_L; – – – –, C_D.

downstream where $\overline{\alpha}$ reaches a value of 0.05 after its initial increase. This figure also shows the maximum $\overline{\alpha}$ obtained in the near wake. As the cavitation number decreases, it is expected that more vapour will be formed in the wake. Interestingly, the $\overline{\alpha}_{max}$ is higher for $\sigma = 1.0$, when compared to $\sigma = 0.7$. This is due to the effect of the low-frequency cavity detachment when $\sigma = 0.7$, which will be discussed in detail in § 5.6. The root mean square values of void fraction are plotted in figure 14(*b*) and show a trend similar to the mean value. The mean cavity length as a function of cavitation number is shown in figure 14(*c*) and shows that the length increases as the cavitation number is reduced. The plot also shows the mean cavity length as a function of a modified cavitation number $\sigma_m = (p - p_v)/(0.5\rho u_{max}^2)$. Here, u_{max} is the maximum mean velocity in the boundary layer, which is obtained from figure 12(*a*). This modification was first suggested by Rao & Chandrasekhara (1976), who observed that, when the mean cavity length was plotted against σ, a family of curves were obtained for different Reynolds numbers for cavitating flow over a circular cylinder. Hence they introduced the modified cavitation number, which unified the different families of curves onto a single curve. We observe in figure 14(*c*) that the mean cavity length obtained at a lower Reynolds number also collapses onto this experimental fit if the modified cavitation number is used. Given that the experimental fit is obtained purely based on experiments at high Reynolds number (typically 10^5), it is interesting to see that the data from our low-Reynolds-number simulations also collapse onto this curve.

5.5. *Unsteady loads on the cylinder*

Figure 15 shows the unsteady characteristics of the flow in the form of lift and drag history and their corresponding spectra in the frequency domain. The Strouhal number (fD/u_∞, where f is the vortex shedding frequency) computed from the lift and drag histories is tabulated in table 2. Further, it is also verified that the same shedding

Cavitation number (σ)	Strouhal number (from C_L)	Strouhal number (from C_D)
2.0	0.1984	0.3967
1.0	0.1603	0.3206
0.7	0.1526	0.3042
0.5	0.08–0.103	0.2231

TABLE 2. Strouhal numbers obtained from lift and drag coefficient history.

Strouhal number is obtained from the pressure history at three different points at $x/D = 2.5$, 5.0 and 10.0 along the wake centreline (not shown here). The lift and drag curve for $\sigma = 1.0$ in figure 15(*a*,*d*) is periodic (but not sinusoidal as in a single-phase flow) and the cavitating vortices are shed at periodic intervals. The cavitating vortices in $\sigma = 1.0$ shed directly from the body and hence this flow belongs to the cyclic cavitation category. The Strouhal number for $\sigma = 1.0$ is reduced to 0.16 from a value of 0.19 for a single-phase flow at $Re = 200$. Apart from the primary peaks, which correspond to the pressure variation due to vortex shedding, smaller secondary peaks are also observed in the lift curve. These secondary peaks correspond to those instants when a pressure wave impinges on the cylinder. The lift and drag histories for $\sigma = 0.7$ and 0.5 in figure 15(*b*,*e*) and (*c*,*f*) are quasi-periodic, with more than one frequency being observed. Further, the magnitude of the fluctuations is also reduced when compared to $\sigma = 1.0$, pointing to a more steady behaviour near the cylinder as the flow cavitates more. The cavitating vortex does not shed directly from the body as in $\sigma = 1.0$, but from the trailing edge of the cavity attached to the cylinder. The Strouhal number corresponding to this shedding is 0.15 for $\sigma = 0.7$. At $\sigma = 0.5$, the vortex shedding becomes intermittent and a peak is observed between Strouhal numbers of 0.08 and 0.11. Thus decreasing cavitation number has two main effects on the unsteady loads: vortex shedding frequency is reduced, the mechanism of which will be discussed in § 5.7; and the magnitude of unsteady loads on the cylinder is also reduced, pointing to a more steady behaviour near the cylinder.

Figure 16 illustrates the dynamics of vapour cloud collapse and the subsequent pressure wave formation for $\sigma = 1.0$. This figure shows void fraction contours, pressure contours and the corresponding instant in the load cycle for various instants of time. Figure 16(*a*,*e*,*i*) shows the impending collapse of the vapour cavity and figure 16(*b*,*f*,*j*) shows the subsequent collapse of the cavity, leading to two separate smaller regions of vapour denoted as Cav 1 and Cav 2. This collapse causes a pressure wave (Wav 1) that propagates outwards. By this time, the separated cavity (Cav 2) also collapses, leading to another pressure wave (Wav 2), as shown in figure 16(*c*,*g*,*k*). Figure 16(*d*,*h*,*l*) shows the fully formed vapour cavity on the top half of the cylinder and this entire cycle repeats itself. This process of cloud collapse and pressure wave formation is similar for both $\sigma = 0.7$ and 0.5, except for a low-frequency detachment of the vapour cavity in the wake in these two cases.

5.6. *Low-frequency cavity detachment in* $\sigma = 0.7$ *and* 0.5

For $\sigma = 0.7$ and 0.5, in addition to the vortex shedding from the trailing edge of the attached cavity, the entire attached vapour cavity also gets detached as a part of the cycle. As a result, the near wake is cavitation-free for a small interval of time. For $\sigma = 0.7$ this cavitation-free time period is approximately $20tu_\infty/D$ and for $\sigma = 0.5$

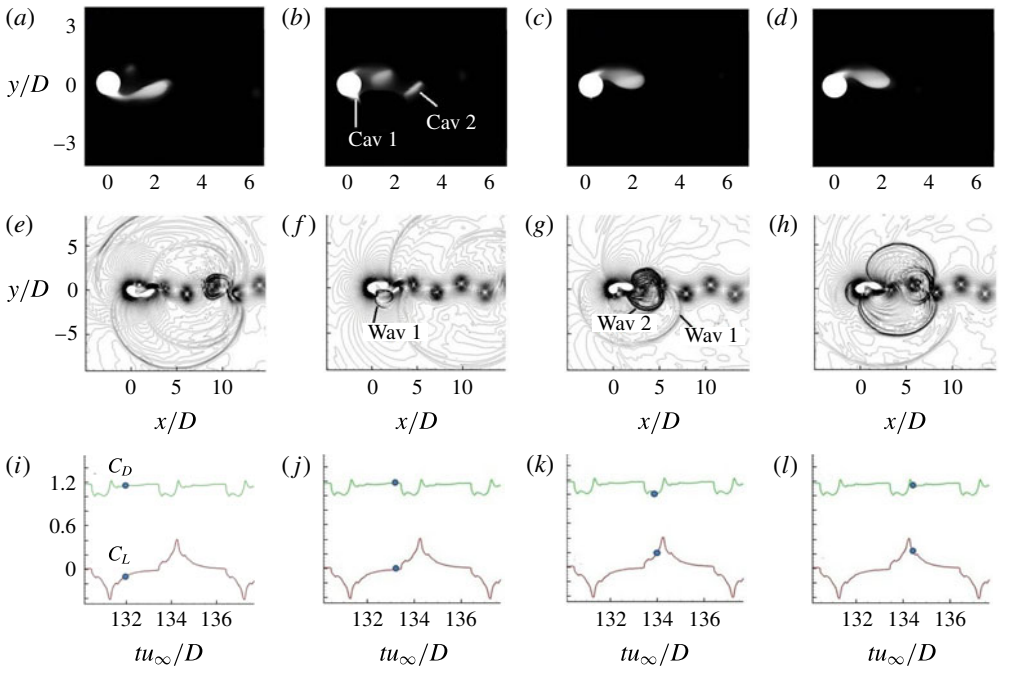

FIGURE 16. (Colour online) Vapour collapse dynamics for $\sigma = 1.0$.

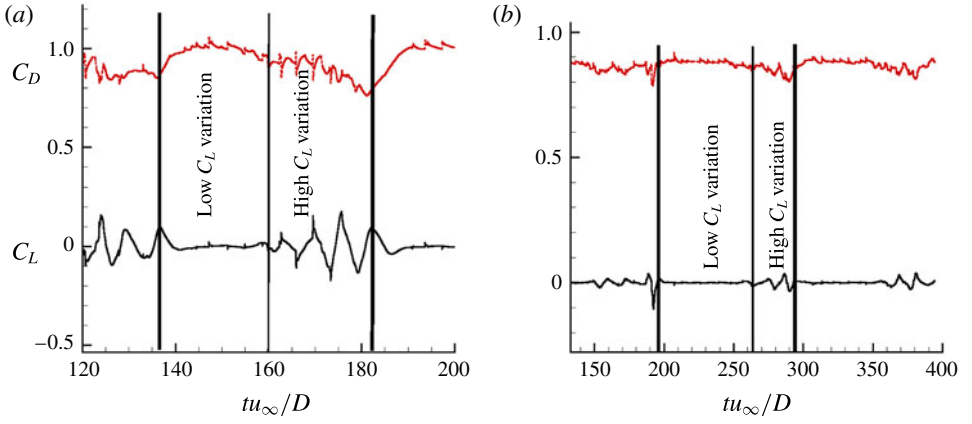

FIGURE 17. (Colour online) Time history of lift showing two phenomena in a single cycle for (*a*) $\sigma = 0.7$ and (*b*) $\sigma = 0.5$: ——, C_L; – – – –, C_D.

it is approximately $30tu_\infty/D$. The frequency corresponding to this detachment can be observed as a peak in the drag spectra in figure 15(*b*,*c*) and is computed to be 0.0218 for $\sigma = 0.7$ and 0.0102 for $\sigma = 0.5$. The lift curves in figure 17(*a*,*b*) suggest that there are two distinct parts within one cycle: one with a relatively low variation in C_L and another with a higher variation in C_L. The first part with low C_L variation corresponds to the time when the vapour cavity is attached to the body. Since the pressure in the vapour region is close to the vapour pressure, the variation in C_L is

very small. As the vapour cavity detaches, water in the wake causes higher variations in the lift coefficient.

The mechanism behind this detachment is illustrated in figure 18, where a series of snapshots show the presence of a propagating condensation front that causes cavity detachment from the base of the cylinder. Figure 18(*a*,*c*) shows the propagation of the condensation front towards the low-pressure base. This causes the pressure in the base to increase, which can be seen as a small patch of high-density fluid near the base of the cylinder (figure 18*e*). This causes the vapour cavity to detach, as seen in figure 18(*g*). The detached cavities advect downstream, leaving the near-wake cavitation free for a while. The presence of a condensation front can also be seen from the line plots in the figure. The pressure increase and the corresponding void fraction decrease close to $x/d = 2.0$ seen in figure 18(*b*,*d*) is the condensation front. Figure 18(*f*,*h*) also shows the presence of high-density (low-void-fraction) fluid near the base once the cavity detaches.

The low-frequency cavity detachment in $\sigma = 0.7$ means that the entire near wake is cavitation-free for a while. This effectively reduces the time-averaged void fraction in those regions where cavitation is absent during some part of the cycle. Hence the maximum time-averaged void fraction of $\sigma = 0.7$ is lower than that of $\sigma = 1.0$, as seen in figure 14(*a*). This cavitation-free period is a substantial part of one cycle for $\sigma = 0.7$ ($20tu_\infty/D$ out of $45tu_\infty/D$) when compared to the $\sigma = 0.5$ ($30tu_\infty/D$ out of $100tu_\infty/D$) where the cavitation-free period is for a lesser amount of time in the cycle. Thus this effect is not pronounced in $\sigma = 0.5$ when compared to $\sigma = 0.7$.

5.7. *Mechanism of vortex shedding frequency reduction*

At low Reynolds number, the vorticity transported into the wake from the boundary layers on the cylinder is diffused away from the shear layer predominantly by viscous action. As the Reynolds number increases, viscous diffusion alone cannot keep up with the increased vorticity production from the boundary layers, and so vortices break away at regular intervals, constituting vortex shedding (Strykowski & Sreenivasan 1990). Gerrard (1966) observed vortex street formation to be a function of two length scales: the formation length and diffusion length. The formation length l_f is defined as the distance downstream of the cylinder along the centreline where the streamwise velocity fluctuations are maximum, and the diffusion length l_d is the width to which the free shear layers diffuse. He found that the vortex shedding frequency could be reduced if the shear layer vorticity was reduced over a critical diffusion length, which in turn increases the formation length.

In order to understand the mechanism of vortex shedding suppression due to cavitation, we first compute the formation length (l_f) by plotting the streamwise velocity fluctuations in figure 19 for $\sigma = 2.0$, 1.0, 0.7 and 0.5. The formation length is seen to increase with decreasing cavitation number, which signifies a reduction in shedding frequency (Gerrard 1966). It is also worthwhile to note that the magnitude of the streamwise velocity fluctuation also increases as the flow cavitates. This points to higher oscillations at the cavity closure as σ is lowered. Also shown in figure 19 are the instantaneous vorticity contours, showing fewer vortices being shed over a given distance as the cavitation number is reduced.

Figure 20 shows the mean vorticity distribution in the top half of the shear layer. The arguments presented here can be applied to the bottom half also by symmetry. Note that the magnitude of negative vorticity in the top shear layer decreases progressively as the cavitation number decreases. Thus cavitating flow has

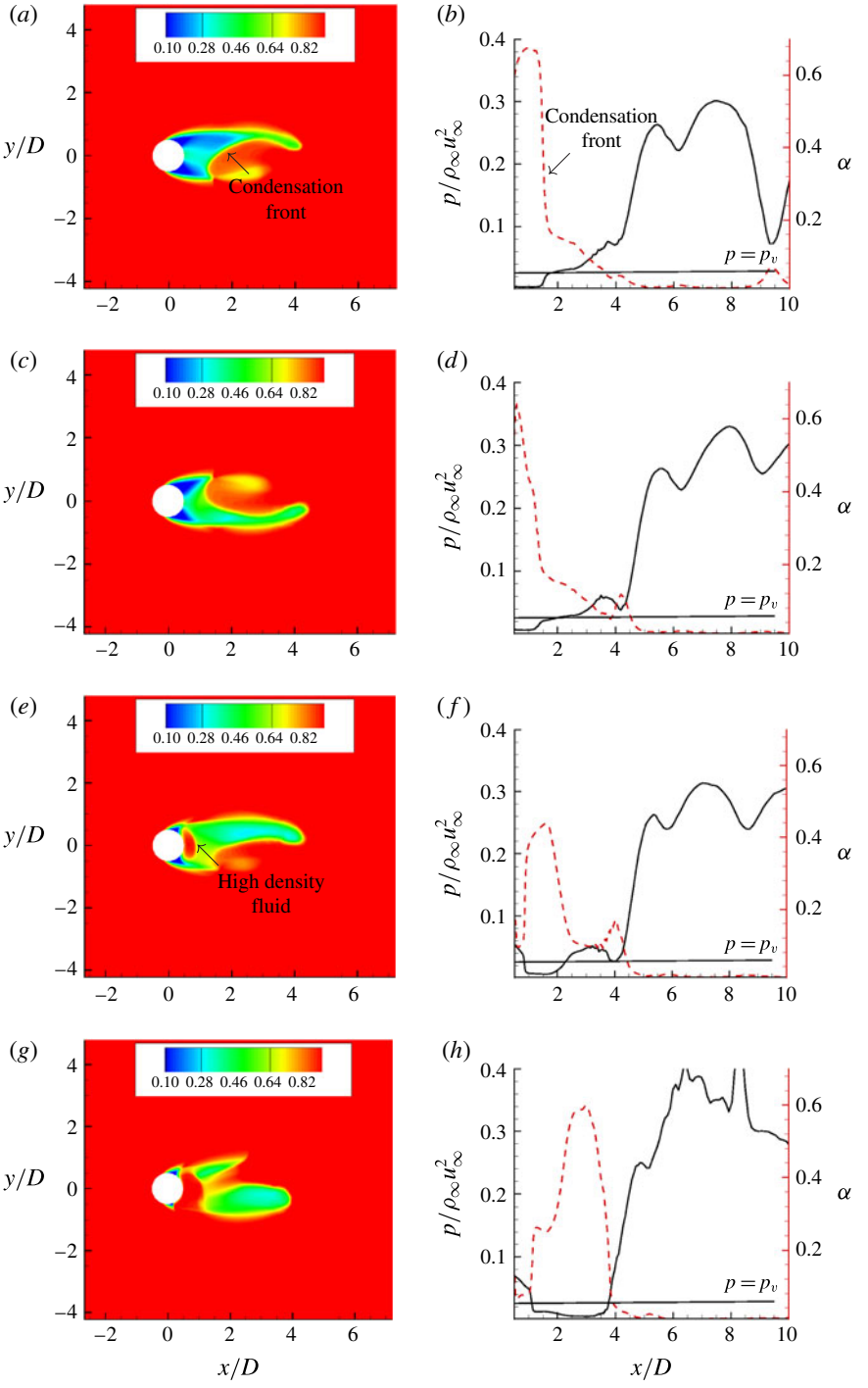

FIGURE 18. (Colour online) (*a*,*c*,*e*,*g*) Density contours at four time instants illustrating a propagating condensation front causing cavity detachment. (*b*,*d*,*f*,*h*) Variation of pressure and void fraction along the wake centreline at four time instants.

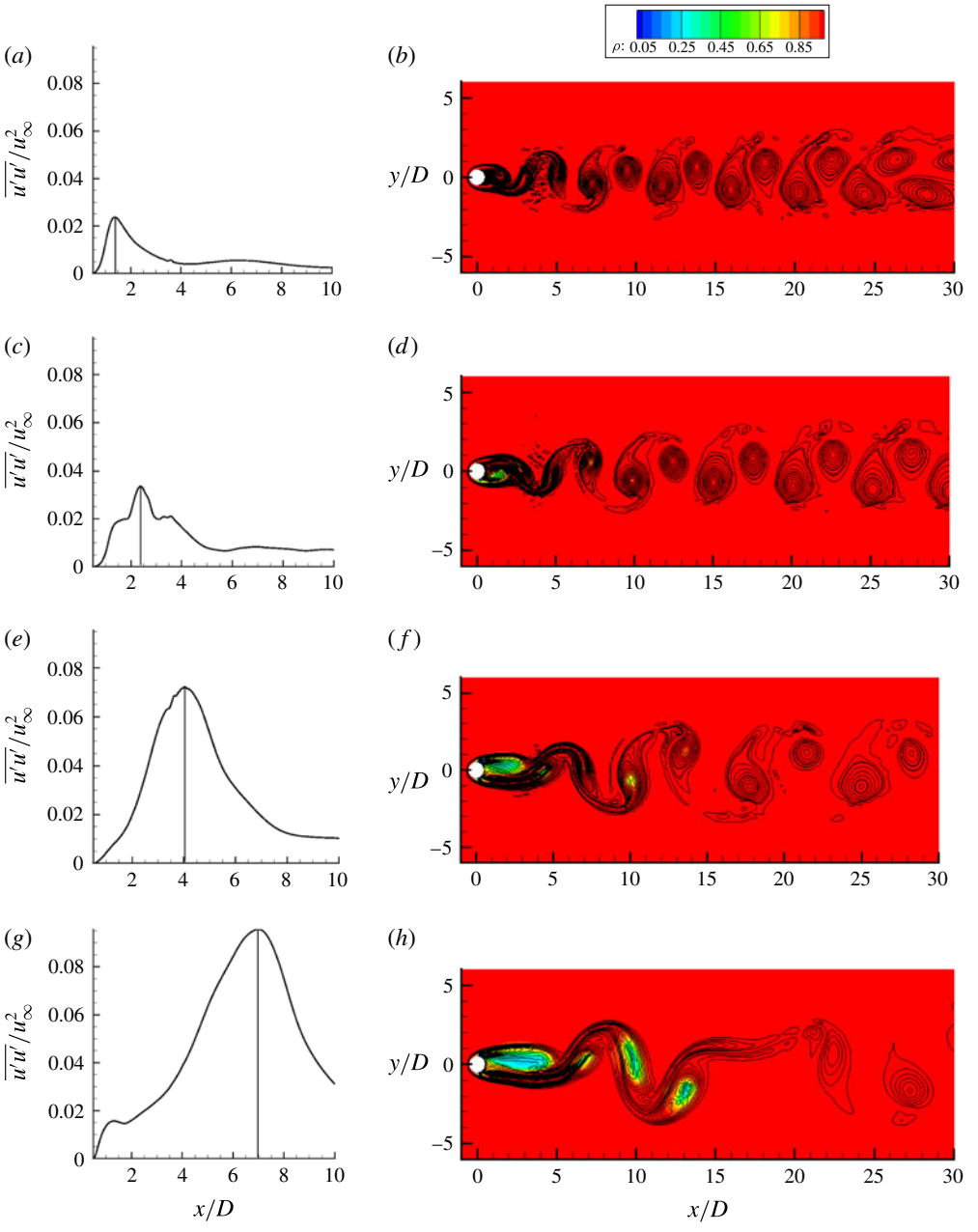

FIGURE 19. (Colour online) (*a*,*c*,*e*,*g*) Formation length and (*b*,*d*,*f*,*h*) instantaneous vorticity contour coloured with density for: (*a*,*b*) $\sigma = 2.0$, $l_f/D = 1.45$; (*c*,*d*) $\sigma = 1.0$, $l_f/D = 2.35$; (*e*,*f*) $\sigma = 0.7$, $l_f/D = 4.19$; and (*g*,*h*) $\sigma = 0.5$, $l_f/D = 7.01$.

lesser vorticity across a given shear layer width and the reason for this reduction is explained below using the vorticity equation,

$$\frac{\partial \boldsymbol{\omega}}{\partial t} = -(\boldsymbol{v}\cdot\boldsymbol{\nabla})\boldsymbol{\omega} + (\boldsymbol{\omega}\cdot\boldsymbol{\nabla})\boldsymbol{v} - \boldsymbol{\omega}(\boldsymbol{\nabla}\cdot\boldsymbol{v}) + \frac{1}{\rho^2}(\boldsymbol{\nabla}\rho\times\boldsymbol{\nabla}p) + \boldsymbol{\nabla}\times\frac{\boldsymbol{\nabla}\cdot\tau}{\rho}. \tag{5.1}$$

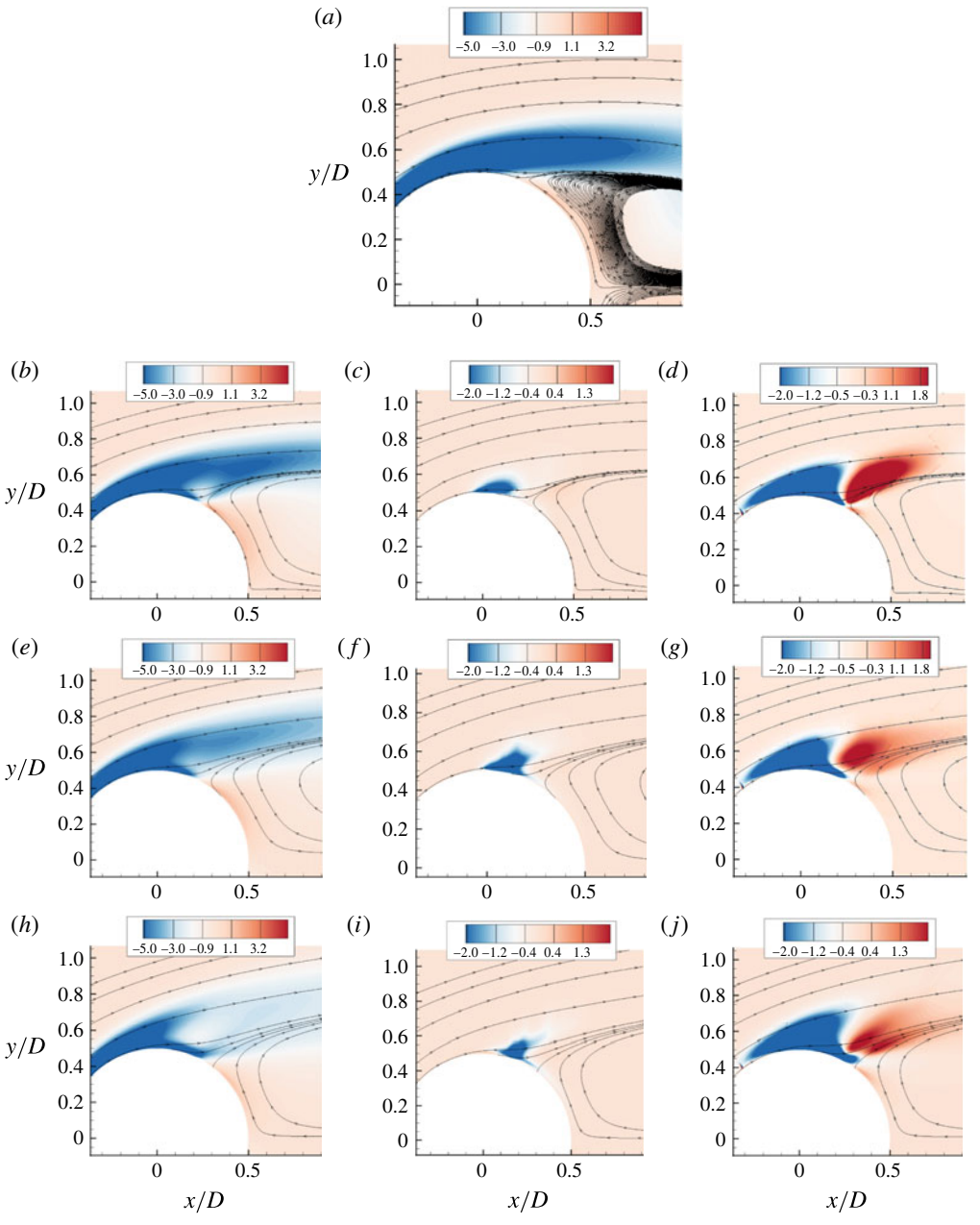

FIGURE 20. (Colour online) Mean vorticity contour (*a*,*b*,*e*,*h*), mean baroclinic vorticity (*c*,*f*,*i*) and mean vorticity dilatation (*d*,*g*,*j*) for (*a*) $\sigma = 2.0$, (*b–d*) $\sigma = 1.0$, (*e–g*) $\sigma = 0.7$ and (*h–j*) $\sigma = 0.5$.

For a constant-density non-cavitating flow, the vorticity dilatation term ($\boldsymbol{\omega}(\boldsymbol{\nabla} \cdot \boldsymbol{v})$) and the baroclinic vorticity ($(1/\rho^2)(\boldsymbol{\nabla}\rho \times \boldsymbol{\nabla}p)$) terms are zero. However, for a cavitating flow, these values are non-zero. Figure 20 shows the contribution of the mean baroclinic vorticity term. At the inception location, baroclinic vorticity is produced

Cavitation number (σ)	Circulation (Γ)	Formation length (l_f/D)
2.0	4.80	1.45
1.0	4.03	2.35
0.7	3.08	4.19
0.5	2.78	7.01

TABLE 3. Values of circulation Γ and formation length l_f.

because pressure becomes a function of both vapour mass fraction and density, thus causing a misalignment between pressure and density gradients. The baroclinic term produces more negative vorticity on the top half for all the cavitating cases thus increasing the total vorticity in the shear layer. The main reason for vorticity reduction is the vorticity dilatation term. As seen in figure 10, there is a large region of positive divergence (expansion) corresponding to the vapour region. The magnitude of vorticity dilatation is also shown in figure 20. Note that this term appears in the right-hand side of the vorticity equation with a negative sign. The blue region corresponds to vorticity dilatation, which reduces the vorticity in the shear layer. The compression region (discussed in § 5.2) causes the vorticity to increase downstream, shown as the red contours: however, the larger influence of the expansion region results in a net decrease in vorticity.

To quantify the extent of vorticity reduction, the circulation in the shear layer is computed as $\oint \boldsymbol{V} \cdot \mathbf{d}\boldsymbol{l}$ over a rectangular domain from $0.5 < x/D < 4.0$ and $0 < y/D < 1.0$, where the centre of the cylinder lies at the origin. As the flow cavitates more, the amount of circulation decreases, pointing to reduced vorticity in the shear layer. Table 3 lists the values of circulation and the corresponding formation lengths for all the cases. Thus the presence of vapour in the wake causes dilatation of vorticity, resulting in a reduction of the vortex shedding frequency.

6. Effect of initial void fraction

In this section, we discuss the effect of initial void fraction (α_0) on the flow field by simulating $\sigma = 1.0$ flow with $\alpha_0 = 0.005$ and comparing it to $\alpha_0 = 0.01$. The initial void fraction values of 1 % and 0.5 % are large compared to those used in controlled experiments. However, these values are chosen to reduce the acoustic stiffness of the system. The main effect of changing α_0 is the change in free-stream speed of sound. At a temperature of 293 K and a pressure of 1 bar, the speed of sound in a mixture with $\alpha_0 = 0.01$ is 100.24 m s^{-1}, while that at $\alpha_0 = 0.005$ is 141.07 m s^{-1}. Hence pressure waves propagating in the medium will travel at these substantially different speeds, which would affect related phenomena. However, phenomena that are driven largely by inertia (e.g. cavitation in shear layer, vortex shedding) are not expected to vary significantly.

6.1. *Mean C_p and C_f distributions on the cylinder*

The time-averaged C_p distribution and C_f distribution are shown as a function of θ in figure 21(*a*,*b*) for both $\alpha_0 = 0.01$ and 0.005. Note that neither C_p nor C_f vary significantly for different α_0. The time-averaged load on a cylinder is predominantly due to the alternate vortex shedding, which is not affected significantly by change in

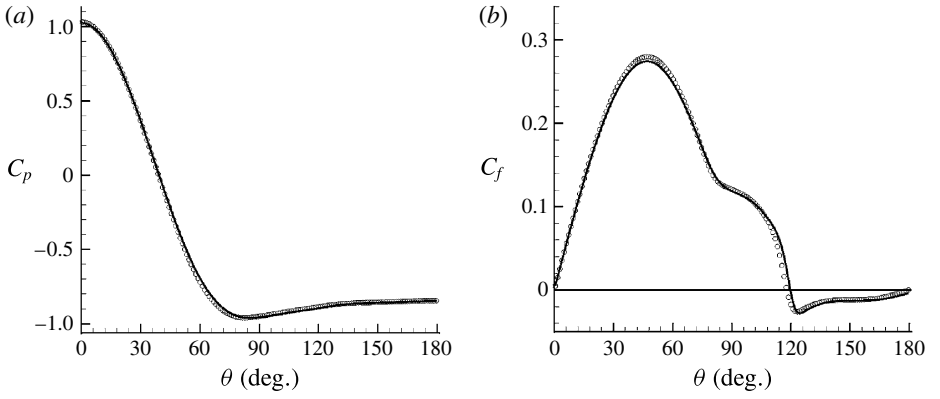

FIGURE 21. (*a*) Time-averaged C_p distribution on the cylinder, and (*b*) time-averaged C_f distribution on the cylinder: ——, $\alpha_0 = 0.01$; ○, $\alpha_0 = 0.005$.

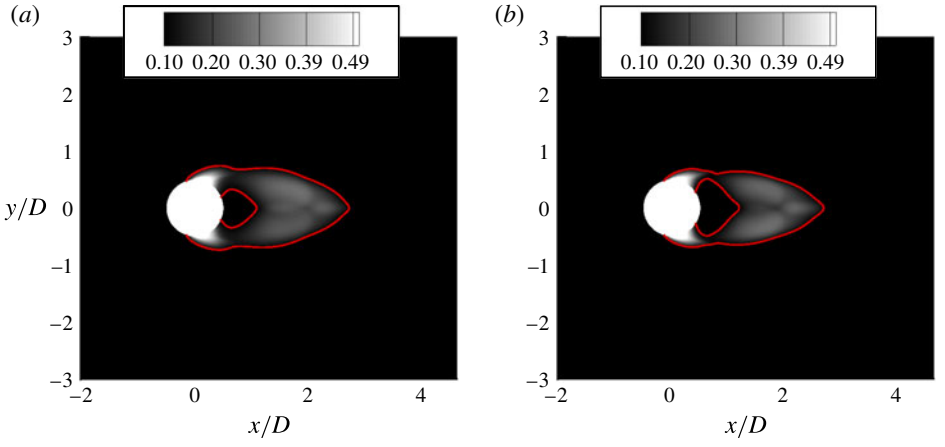

FIGURE 22. (Colour online) Mean void fraction contour for (*a*) $\alpha_0 = 0.01$ and (*b*) $\alpha_0 = 0.005$.

acoustic speed. The inflection point (at $\theta = 80°$) in the C_f curve that indicates the cavity inception location (as discussed in § 5) also remains unchanged between the two flows. Figure 22 shows the mean void fraction contours for both the flows. The cavity shape and cavity length ($l_{cav}/D = 2.71$) remain largely unaffected. According to the continuity equation, $\partial u_j/\partial x_j = -(1/\rho)(\mathrm{D}\rho/\mathrm{D}t)$, the divergence of velocity depends on the material derivative of density. The main contribution to density change comes from the phase change, which has a time scale of its own due to the finite rate. Since phase change does not occur on the acoustic scale, changing the speed of sound does not significantly affect the divergence of velocity and hence its interplay with the boundary layer is also largely unaffected. Figure 23 shows contours of mean velocity divergence for both $\alpha_0 = 0.01$ and 0.005. The contours are identical, confirming the fact that velocity divergence is not affected by the initial void fraction.

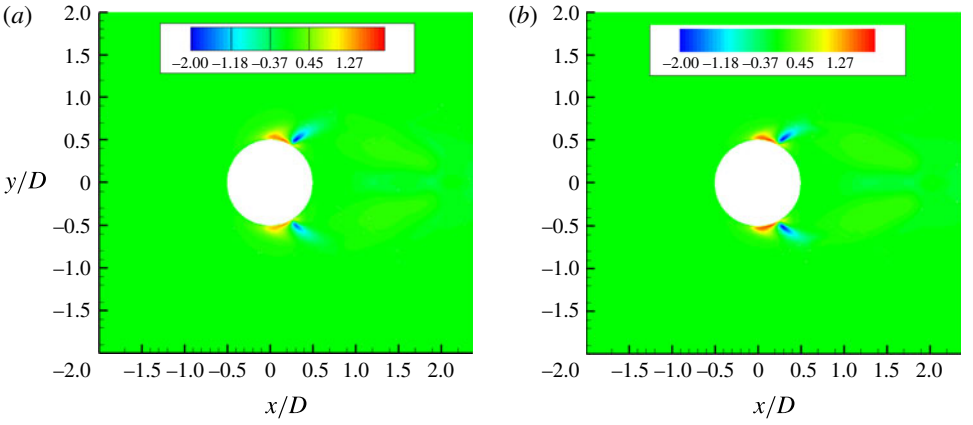

FIGURE 23. (Colour online) Mean velocity divergence contour for (*a*) $\alpha_0 = 0.01$ and (*b*) $\alpha_0 = 0.005$.

6.2. *Unsteady loads on the cylinder*

The effect of changing α_0 on the unsteady loads is investigated in figure 24(*a*,*b*). The lift and drag history shown in figure 24(*a*) is very similar to the $\alpha_0 = 0.01$ case (figure 15*a*), and the corresponding shedding Strouhal number obtained in figure 24(*b*) is also unaltered. The only effect of reducing α_0 below 0.005 is an increase in the speed of sound in the medium, effectively reducing the Mach number of the flow, which is not expected to affect the shedding characteristics significantly. Figure 24(*c*) shows a single lift and drag cycle for both the cases. It can be observed that the time period and the magnitude of the primary peak of the cycle are the same. However, the pressure wave impingement causes a higher pressure increase for $\alpha_0 = 0.005$, leading to a larger secondary peak, as can be observed from the inset in figure 24(*c*). This implies that a stronger pressure wave is produced due to vapour collapse for $\alpha_0 = 0.005$ and this aspect is investigated further.

6.3. *Pressure waves due to cavity collapse*

To understand the effect of α_0 on pressure waves, the pressure history at three different locations ($x/D = 2.5$, 5.0 and 10.0) along the wake centreline is examined in figure 25 for both the flows. There are adequate numbers of time samples ($\approx$50) within each peak to resolve it accurately. Note that higher values for pressure peaks are obtained for $\alpha_0 = 0.005$. This change in pressure can be explained as follows. For an inviscid, isentropic flow, the pressure perturbation due to an acoustic wave is

$$p - \overline{p} = \overline{c}^2(\rho - \overline{\rho}) = \overline{\rho}\,\overline{c}^2 S = Z\,\overline{c} S, \tag{6.1}$$

where $\overline{c}$ is the mean speed of sound, $Z \equiv \overline{\rho}\,\overline{c}$ is the acoustic impedance and $S \equiv (\rho - \overline{\rho})/\overline{\rho}$ is the condensation ratio. The time history of pressure perturbation scaled by $\overline{\rho}\,\overline{c}^2$ is shown in figure 26(*a*,*b*) for both the cases. It can be observed that the peak values of the scaled pressure perturbation are similar for both the flows, indicating similar values of condensation ratio S. To obtain the same condensation ratio in a less compressible medium (higher Z and $\overline{c}$), a higher pressure rise would be required, explaining the larger pressure peaks for $\alpha_0 = 0.005$. Thus the major

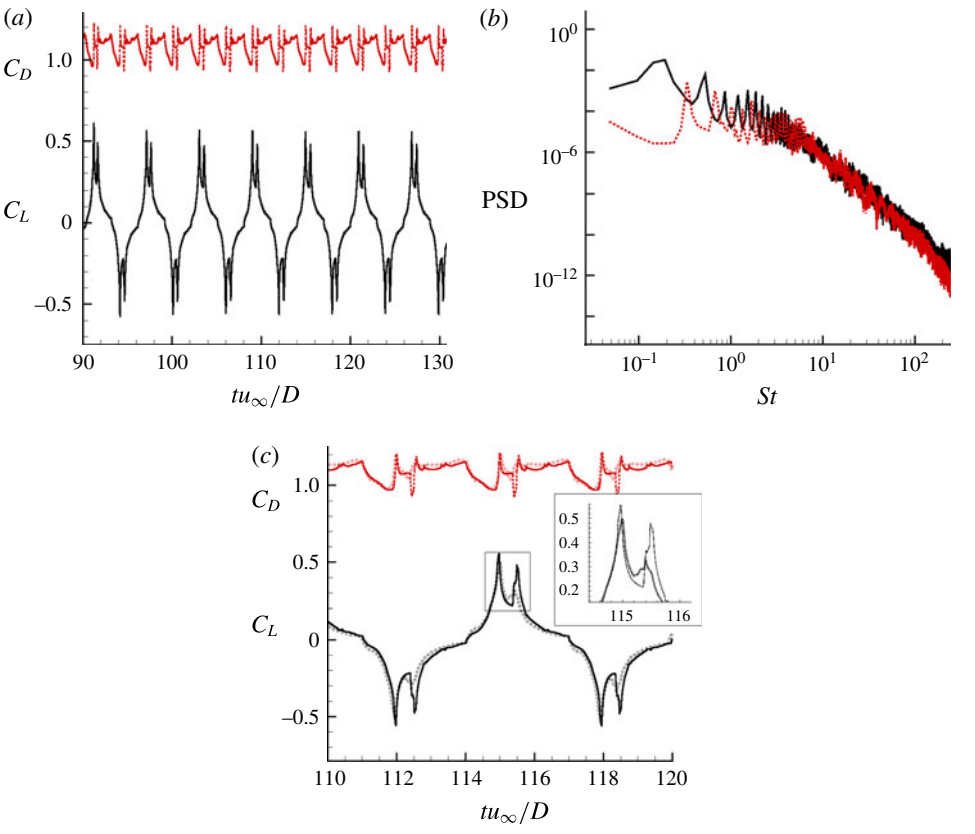

FIGURE 24. (Colour online) (*a*) Lift and drag history for $\alpha_0 = 0.005$. (*b*) Power spectral density for $\alpha_0 = 0.005$: ——, C_L; – – – –, C_D. (*c*) Comparison of a single lift and drag cycle: ○, $\alpha_0 = 0.01$; and ——, $\alpha_0 = 0.005$.

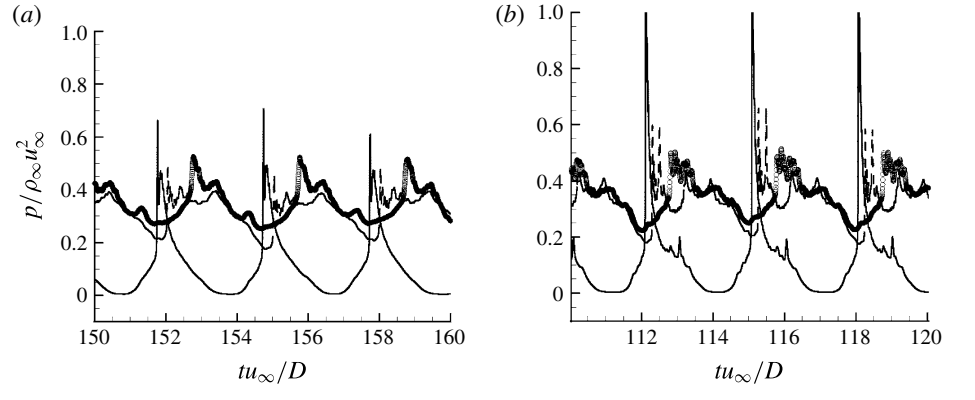

FIGURE 25. Pressure history at three different locations along the wake centreline for (*a*) $\alpha_0 = 0.01$ and (*b*) $\alpha_0 = 0.005$: ——, $x/D = 2.5$; – – – –, $x/D = 5.0$; ○, $x/D = 10.0$.

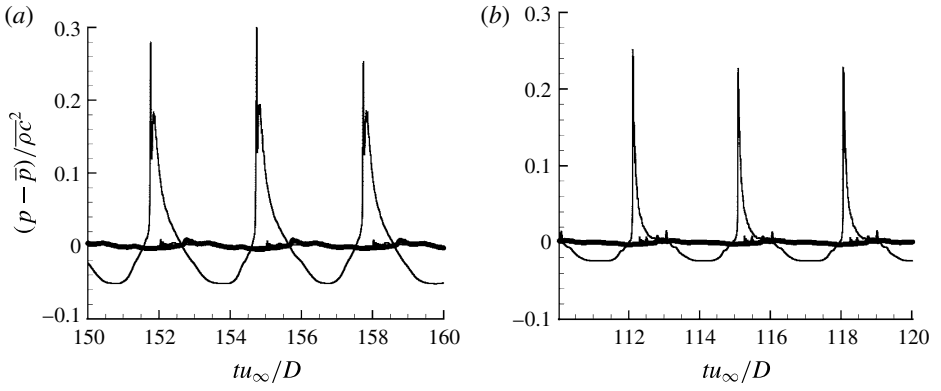

FIGURE 26. Change in condensation ratio at three different locations along the wake centreline for (*a*) $\alpha_0 = 0.01$ and (*b*) $\alpha_0 = 0.005$: ——, $x/D = 2.5$; – – – –, $x/D = 5.0$; ○, $x/D = 10.0$.

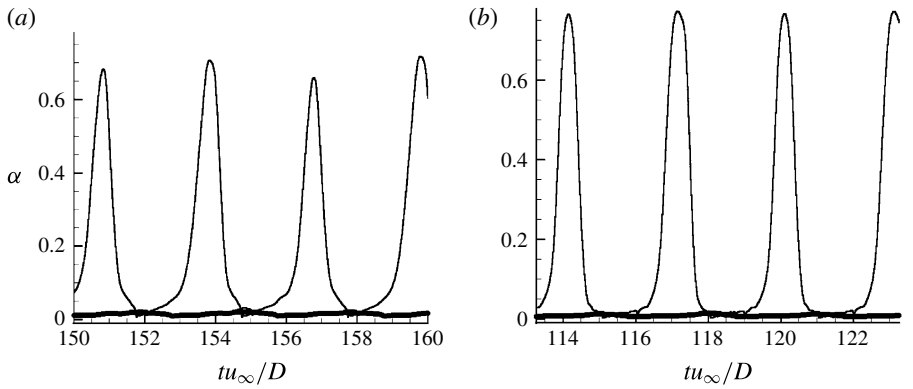

FIGURE 27. Time history of vapour volume fraction at three different locations along the wake centreline for (*a*) $\alpha_0 = 0.01$ and (*b*) $\alpha_0 = 0.005$: ——, $x/D = 2.5$; – – – –, $x/D = 5.0$, ○, $x/D = 10.0$.

consequence of changing α_0 seems to be to produce a pressure wave that has a higher pressure rise across it, but produces the same amount of density change in the medium. The similarity in S for both α_0 can be explained using figure 27, which shows the vapour volume fraction history corresponding to the pressure history in figures 25 and 26. The vapour volume fraction drops from a value of approximately 0.6 to the free-stream value at the time instant where the pressure spike occurs in figure 25. Since the free-stream values are at least an order of magnitude less (0.01 and 0.005) than 0.6, the change in vapour volume fraction produced is almost the same for both the flows, which explains the density change also being similar for both the flows.

The difference in the average speed of a pressure wave as it travels between two points can also be observed from figure 25. Waves move faster when $\alpha_0 = 0.005$ due to the higher speed of sound. The average speed of the pressure wave is computed and tabulated along with the average speed of sound in table 4. To compute these quantities it is assumed that the speed does not change between the probe locations.

Location (x/D)	Initial void fraction (α_0)	Avg. condensation wave speed (u_c/u_∞)	Avg. sound speed (c/u_∞)
2.5–5.0	0.01	8.3	8.0
5.0–10	0.01	6.8	7.0
2.5–5.0	0.005	17.0	18.0
5.0–10	0.005	10.0	9.5

TABLE 4. Average speed of pressure wave and sound speed.

Although this assumption is not strictly valid, it gives a sense of the propagation speed of the pressure waves with respect to the sound speed (c). The expression for the speed of sound in a liquid–gas mixture is obtained using the equation of state and Gibbs equation and is given by

$$\left.\begin{aligned} c^2 &= \frac{C_1 T}{C_0 - \dfrac{C_1}{C_{pm}}}, \\ C_0 &= 1 - (1-Y)\rho K_l T \frac{P_c}{(p+P_c)^2}, \\ C_1 &= R_g Y - K_l (1-Y)\frac{P}{p+P_c}, \\ C_{pm} &= Y C_{pg} + (1-Y) C_{pl}. \end{aligned}\right\} \tag{6.2}$$

The relationship used for the speed of sound follows the established dependence of sound speed on void fraction (Gnanaskandan & Mahesh 2015). It is observed that the pressure waves travel almost at the local speed of sound in the medium.

Pressure fluctuation levels of the two cavitating flows are compared to the pressure fluctuations in a non-cavitating flow in figure 28. The difference in the contours downstream of the cylinder on either side of the centreline is evident. The 'cell'-shaped structures formed in the cavitating cases (figure 28*b*,*c*) are the result of the pressure fluctuations caused by the pressure waves due to cavity collapse, which are absent in a single-phase flow. The structures are localized in space due to the fact that the pressure wave impinges with the vortices only at specific points in space. This interaction causes the residual vapour in the vortex core to collapse, leading to a momentary increase in pressure followed by a recovery back to a lower pressure due to the rotation of the vortices. Since this happens until the pressure waves decay and the vapour in the vortices is destroyed completely, a train of 'cell'-shaped structures can be observed until approximately $20D$. Such behaviour would be absent if the wake only had advecting vortices or propagating pressure waves: it is a result of their interaction. Figure 29 shows the variation of pressure fluctuations along the streamwise direction at three different y locations as marked in figure 28(*b*) for both the cavitating flows. Both the wake centreline plot ($y/D = 0.0$) and the cut through the vortex core ($y/D = 0.7$) show several cycles of cavity growth and collapse, and in each cycle the crest corresponds to the collapse of a bubble and each trough is the cavity at its maximum regrown state. The absence of vapour at $y/D = 2.0$ means that pressure fluctuation change is not as substantial as inside the vortices. The propagation speed of the wave is also different and can be observed from the figure.

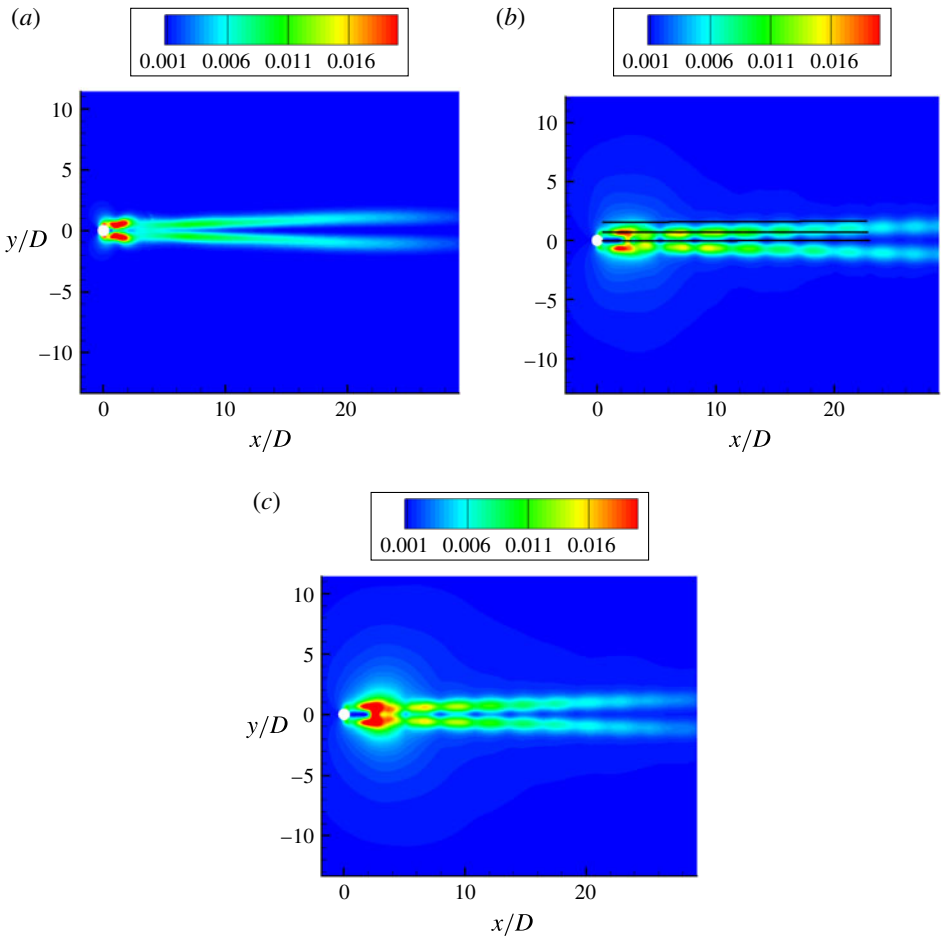

FIGURE 28. (Colour online) Comparison of pressure fluctuation ($\overline{p'^2}$) contour for (*a*) non-cavitating flow, and cavitating flow with (*b*) $\alpha_0 = 0.01$ and (*c*) $\alpha_0 = 0.005$.

Owing to a larger speed of sound, the pressure wave for $\alpha_0 = 0.005$ travels faster and impinges with the vortex at a more upstream location than in the $\alpha_0 = 0.01$ flow.

7. Large-eddy simulation of turbulent cavitating flow at $Re = 3900$

LES of turbulent cavitating flow at $Re = 3900$ and $\alpha_0 = 0.01$ is performed. The topology used for the simulation is similar to the lower-Reynolds-number cases; the grid however is 3D and more refined in the near wake. The averaged statistics are obtained over 10 shedding cycles and satisfactory convergence is obtained in the near-wake region. The number of samples is further increased by averaging along the spanwise direction and also about the wake centreline to improve convergence. Figure 30 shows the instantaneous vortical structures in the form of Q-criterion coloured by void fraction; 3D flow structures of varying scales can be observed. The shear layer breaks up into smaller spanwise structures. The flow structures in the near wake, especially in the vapour cavity, appear to be larger when compared to the flow structures observed by Verma & Mahesh (2012) (figure 16 in their paper)

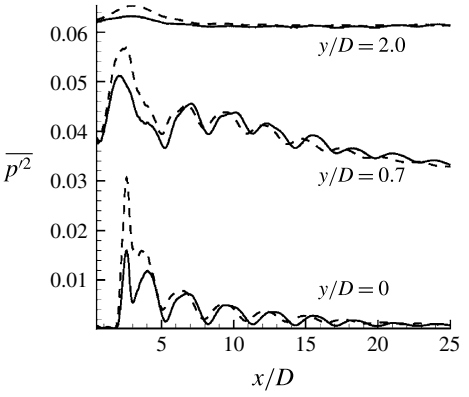

FIGURE 29. Comparison of pressure fluctuations as a function of downstream distance at three different locations in the wake: ——, $\alpha_0 = 0.01$; – – – –, $\alpha_0 = 0.005$. The curves at $y/D = 0.7$ and $y/D = 2.0$ have been shifted along the y axis by 0.03 and 0.06, respectively.

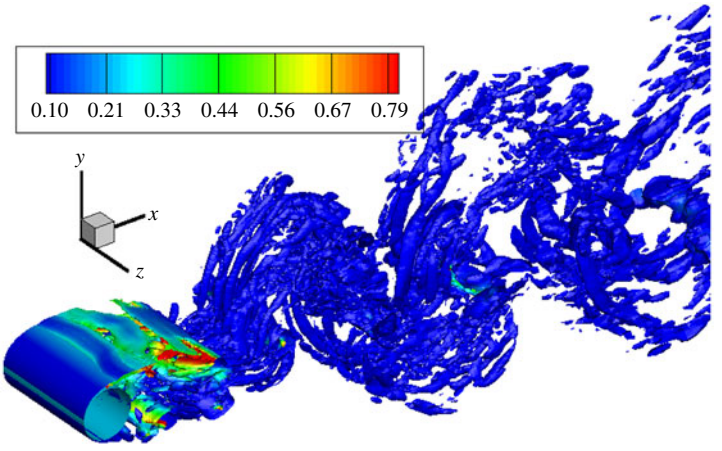

FIGURE 30. (Colour online) Isocontours of $Q = 2$ coloured by void fraction.

in single-phase flow. This is because of the effective lowering of Reynolds number by the presence of vapour. Further, small vapour pockets can be seen trapped in the smaller-scale vortices downstream of the wake. Although the flow is 3D inside the vapour cavity immediately downstream, breakdown to finer scales occurs downstream of the cavity closure. Figure 31 shows instantaneous contours of Mach number, showing supersonic Mach numbers in the shear layer. Cavitation in wake vortices also causes locally supersonic Mach numbers there. The contour lines of pressure show distorted fronts of pressure waves. Turbulence causes different points in the wave fronts to have different speeds, resulting in their distortion.

7.1. *Comparison of $Re = 3900$ cavitating flow to $Re = 200$ cavitating flow*

Figure 32 compares the mean void fraction for $Re = 3900$ to the $Re = 200$ flow. There are minor differences in the cavity shape; the major change, however, is the fact that vapour is distributed uniformly in the wake for the turbulent case as opposed to only

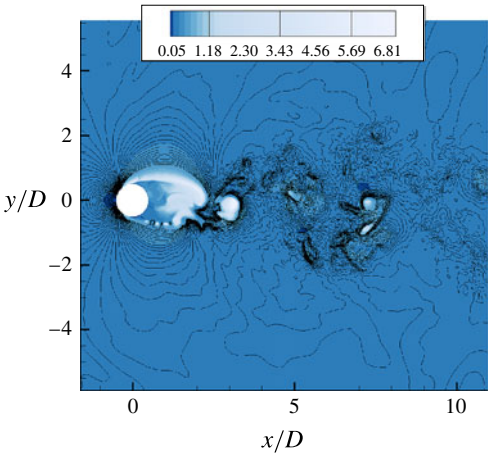

FIGURE 31. (Colour online) Instantaneous Mach-number contours superimposed with lines of pressure.

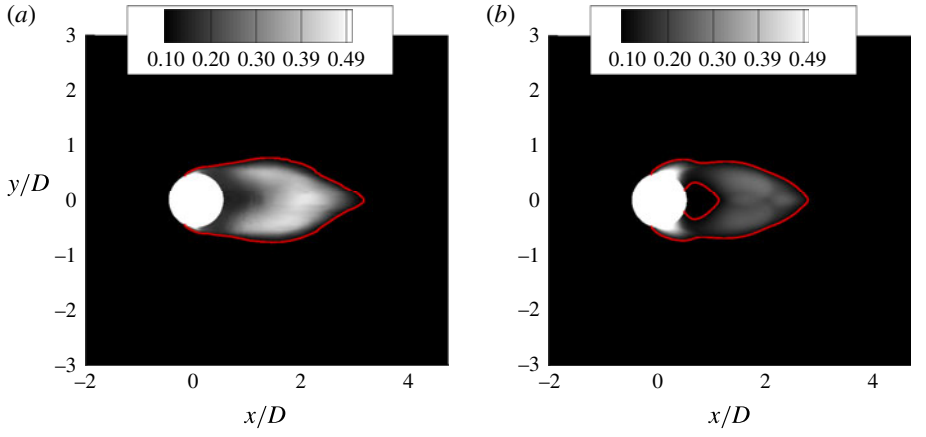

FIGURE 32. (Colour online) Mean void fraction contour for (*a*) $Re = 3900$ and (*b*) $Re = 200$.

in the vortices for the laminar case. The length of the cavity (l_{cav}/D) is 3.04 for the high-Reynolds-number flow, while it is only 2.71 for the low-Reynolds-number flow. Also note the presence of a larger fraction of vapour in the wake for $Re = 3900$. Thus increasing Reynolds number at the same cavitation number makes the flow cavitate more, resulting in a larger cavity dimension. This observation is also in line with that of Rao & Chandrasekhara (1976). The presence of an increased amount of vapour also affects the C_p and C_f distributions. Figure 33(*a*,*b*) compares the time-averaged C_p and C_f distributions of $Re = 3900$ at $\sigma = 1.0$ with the $Re = 200$ flow at the same cavitation number. Also shown in the figure are the C_p and C_f distributions from the single-phase flow at $Re = 3900$, which will be discussed in § 7.2. When compared to the $Re = 200$ flow, the minimum C_p location is shifted upstream, pointing to the inception location moving upstream. The magnitude of the minimum C_p is also reduced in the $Re = 3900$ flow, which is also consistent with the increased amount of vapour. The C_f curve for the $Re = 3900$ flow in figure 33(*b*) shows a different behaviour when compared

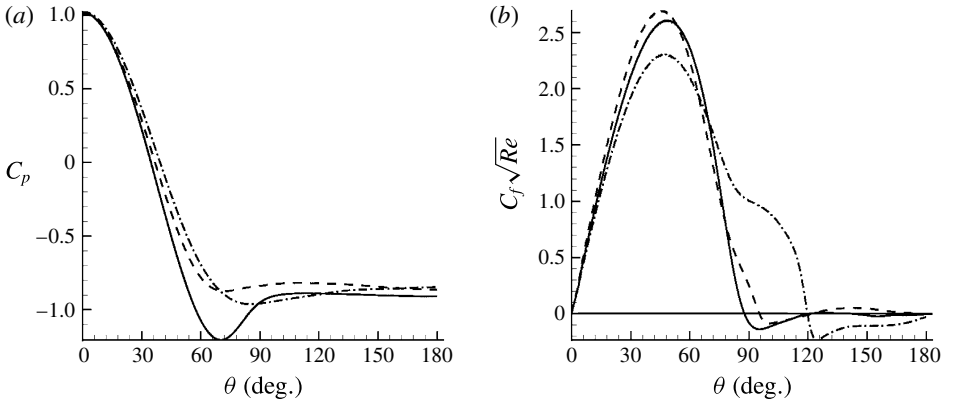

FIGURE 33. (*a*) Time-averaged C_p distribution along the cylinder and (*b*) time-averaged C_f distribution along the cylinder: ——, $Re = 3900$ single-phase flow; – – – –, $Re = 3900$ cavitating flow; and – · – · –, $Re = 200$ cavitating flow.

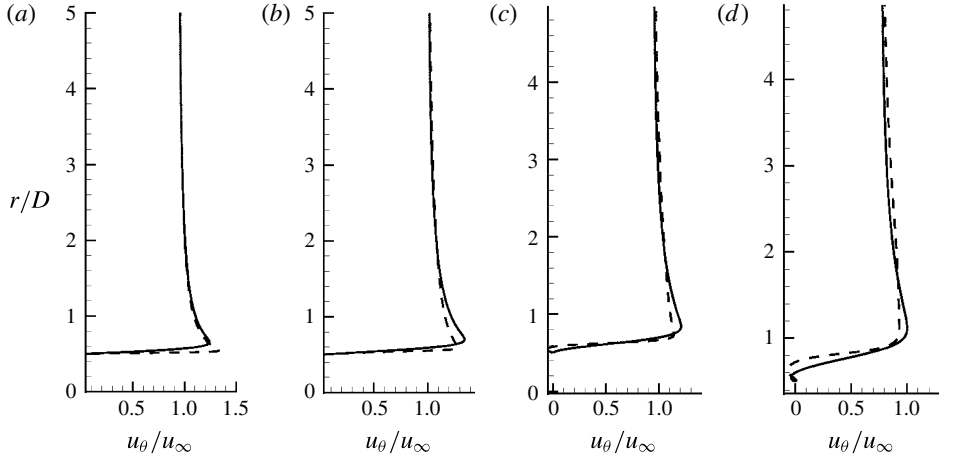

FIGURE 34. Boundary layer profile at four azimuthal locations of (*a*) $\theta = 70°$, (*b*) 90°, (*c*) 110° and (*d*) 130°: ——, $Re = 200$; and – – – –, $Re = 3900$.

to the $Re = 200$ flow. The main difference is that there is a marked difference in the inflection point in the C_f curve. This is due to the fact that the deceleration upstream of the inception location and acceleration downstream of inception caused by cavitation explained in § 5.3 is subdued at $Re = 3900$ when compared to $Re = 200$ due to 3D effects. This also results in the separation location being shifted upstream (95°) for the $Re = 3900$ flow since the acceleration effect present in the $Re = 200$ flow is now reduced.

The mean boundary layer evolution of the high-Reynolds-number flow is compared with the low-Reynolds-number flow in figure 34. At an azimuthal location of 70°, the $Re = 3900$ flow has a higher magnitude for maximum velocity, which is consistent with the reduced amount of deceleration due to cavitation inception. Further, the location of maximum velocity is also shifted closer to the wall for the $Re = 3900$ flow. The maximum velocity at 90° is lower for $Re = 3900$ since the flow is closer

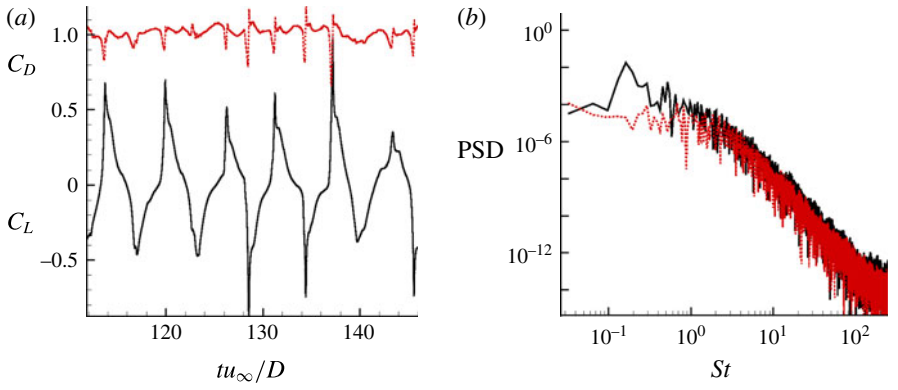

FIGURE 35. (Colour online) (*a*) Lift and drag coefficient history, and (*b*) power spectral density: ——, C_L; – – – –, C_D.

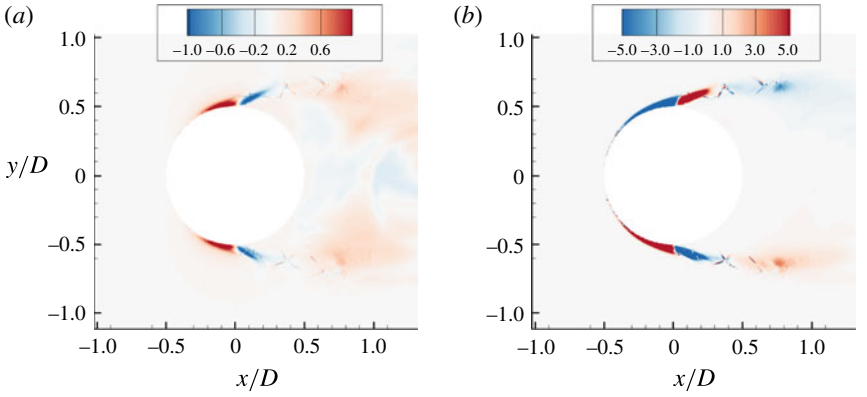

FIGURE 36. (Colour online) (*a*) Mean velocity divergence contour. (*b*) Mean vorticity dilatation contour.

to the separation point and is decelerating much more than the $Re = 200$ flow at the same location. The flow separates at approximately 95° and instances of separated flow can be observed at the downstream locations.

The lift and drag history and their power spectral density are plotted in figure 35. The secondary peaks due to pressure wave impingement are not as prominent as they were in the $Re = 200$ flow. The presence of an increased amount of vapour in the wake presumably reduces the effect of pressure wave impingement. The Strouhal number corresponding to vortex shedding frequency is 0.167, and the reason for the Strouhal number reduction from the single-phase value of 0.2 is very similar to that for the 2D flow and is depicted in figure 36(*a*,*b*). The mean velocity divergence contour shows an expansion region corresponding to vapour formation. A compression region is found immediately downstream of the expansion similar to the $Re = 200$ flow. The expansion region causes vorticity dilatation that can be observed in figure 36(*b*). As in the $Re =$ 200 flow, this vorticity dilatation is the main reason for the vorticity reduction which reduces the vortex shedding frequency.

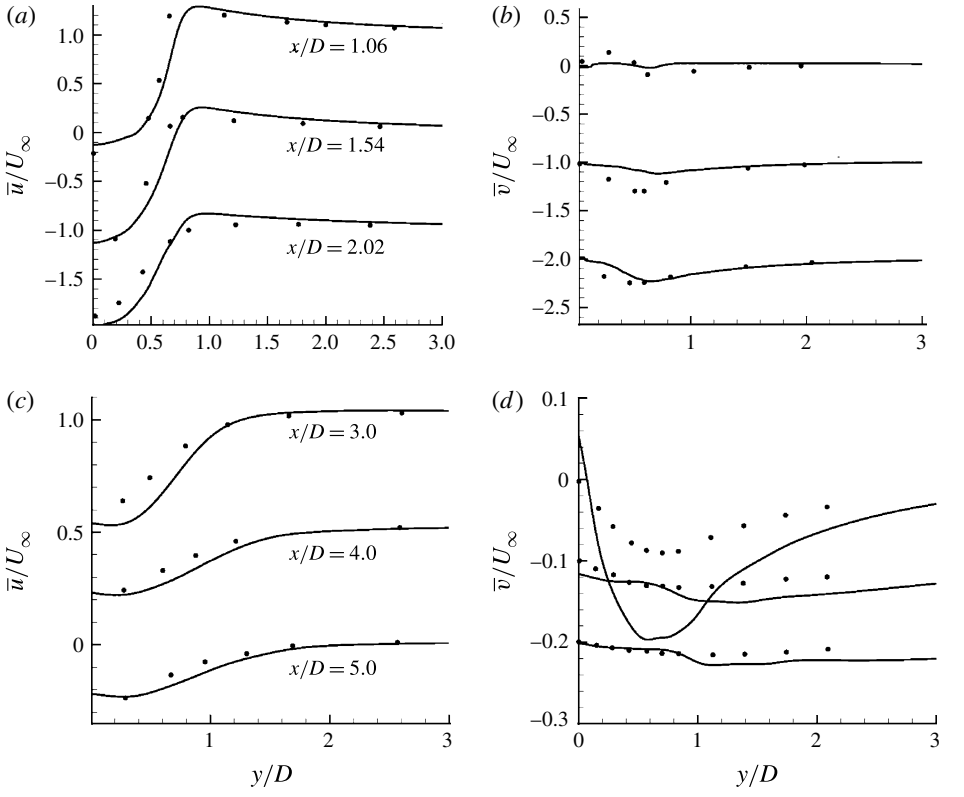

FIGURE 37. Comparison of vertical profiles at streamwise stations downstream of the cylinder at $Re = 3900$: ●, Verma & Mahesh (2012); ——, present results.

7.2. *Comparison of* $Re = 3900$ *cavitating flow to* $Re = 3900$ *non-cavitating flow*

Figure 35(*a*,*b*) also compares the C_p and C_f distributions of $Re = 3900$ cavitating flow with that of the single-phase results of Verma & Mahesh (2012) at the same Reynolds number. Cavitation decreases the magnitude of minimum C_p when compared to the single-phase C_p and the flattening of the C_p curve is due to the presence of vapour, similar to the discussion in § 5.1. The C_f curve comparison shows that the separation location is shifted downstream compared to the single-phase flow. The reason for this shift is the same as discussed in § 5.3.

Figures 37 and 38 compare the mean velocity profiles and turbulence intensity profiles, respectively, in the wake for the cavitating case at $Re = 3900$ to the single-phase results of Verma & Mahesh (2012) at the same Reynolds number. The streamwise velocity profiles at all stations show a wider wake profile for the cavitating flow. The station $x/D = 3.0$ shows the maximum difference in the vertical velocity profile since it corresponds to the cavity closure region. Inside the cavity (except at $x/D = 1.06$), larger values of vertical velocity are obtained. The maximum value for $\overline{u'u'}$ occurs downstream $(x/D = 3.0)$, pointing to a larger formation length. Inside the cavity, the values for $\overline{v'v'}$ are much smaller than those obtained for the single-phase flow. However, the cavity closure at $x/D = 3.0$ is highly unsteady with higher fluctuation values in both streamwise and vertical velocities. The $\overline{u'v'}$ curve shows a similar trend to the mean vertical velocity profiles. Overall, cavitation seems

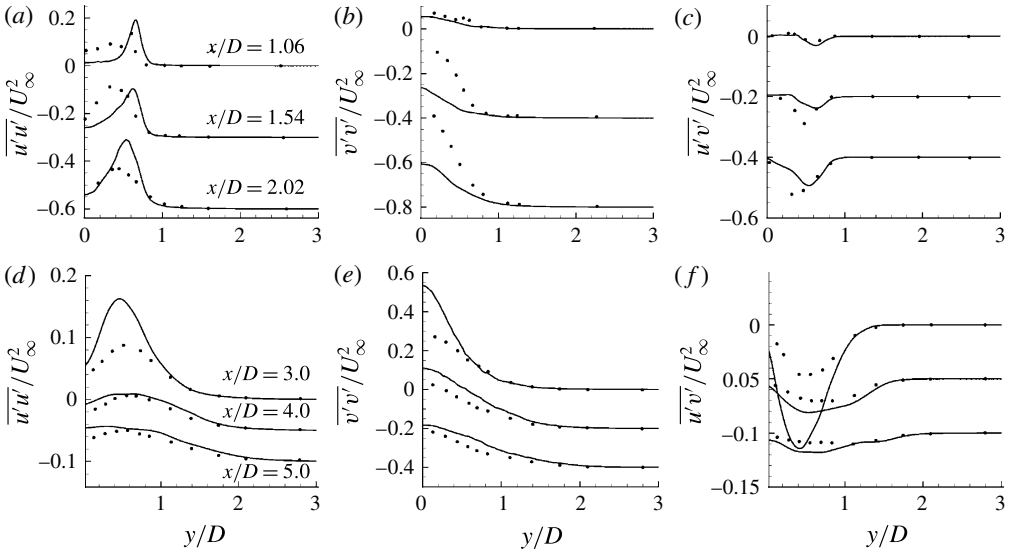

FIGURE 38. Comparison of vertical profiles at streamwise stations downstream of the cylinder at $Re = 3900$: ●, Verma & Mahesh (2012); ——, present results.

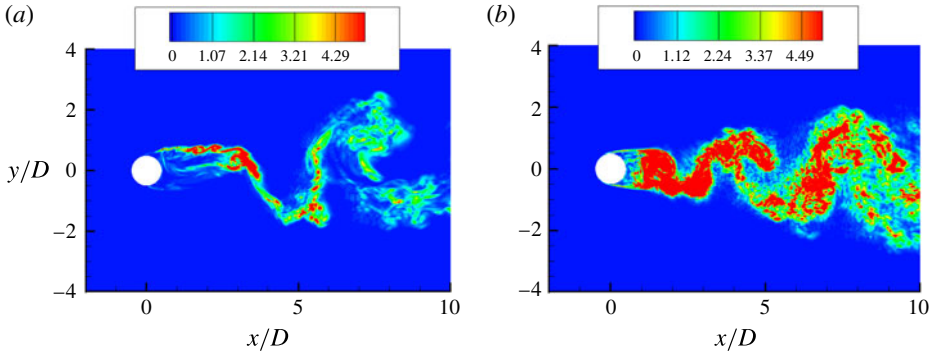

FIGURE 39. (Colour online) Magnitude of vortex stretching in the symmetry plane for (*a*) cavitating flow and (*b*) non-cavitating flow.

to have delayed the complete 3D breakdown of the Kármán vortices by effectively lowering the Reynolds number in the wake. This fact is corroborated in figure 39, which shows the instantaneous magnitude of vortex stretching in the symmetry plane for the multiphase and single-phase flows. Note that the vortex stretching magnitude in the wake is reduced in a cavitating flow. Hence formation of vapour suppresses turbulence, yielding highly correlated spanwise structures in the near wake in figure 30.

8. Summary

A numerical method based on the homogeneous mixture model and characteristic-based filtering is used to study cavitation on a circular cylinder at two Reynolds numbers and several cavitation numbers. The simulated cavitation numbers correspond

to two different regimes based on how the cavity is shed into the wake. The dynamics of cavity formation and collapse leading to pressure waves is captured in the simulations and discussed in detail. A scaling for cavitation number based on maximum velocity in the shear layer is found to collapse the cavity length as a function of cavitation numbers at different Reynolds numbers onto a single curve. In the cyclic regime ($\sigma = 1.0$) of cavitation, the cavity detaches from the body itself at the shedding frequency, while in the transitory regime of cavitation ($\sigma = 0.7$ and 0.5), a low-frequency cavity detachment phenomenon is observed in addition to the shedding frequency. Cavitation is found to significantly modify the vortex shedding frequency, and vorticity dilatation due to vapour is found to be responsible for this shedding frequency reduction. This effect is further verified by computing circulation in the wake, which shows that vorticity reduces as the cavitation number is lowered.

The effect of initial void fraction is assessed. It is found that changing the initial void fraction does not affect the general dynamics of cavity formation. However, the speed of sound is altered significantly and this leads to pressure waves travelling at different speeds. The compressibility and acoustic impedance of the medium are altered but the condensation ratio in the medium shows a similarity for different free-stream void fraction values. The pressure fluctuation contours show spatially local phenomenon due to the interaction between condensation waves and vortices at specific locations in space.

Finally, LES of cavitating flow at $Re = 3900$ reveals that the length of the mean cavity obtained at higher Reynolds number is higher than that at low Reynolds number for the same cavitation number. The vortex shedding frequency is again lower compared to a single-phase shedding frequency and vorticity dilatation is again found to be an important factor in reducing the vorticity in the wake. Cavitation effectively reduces the Reynolds number in the near wake, suppresses turbulence and delays the 3D breakdown of Kármán vortices.

Acknowledgements

This work was supported by the United States Office of Naval Research under ONR grant N00014-11-1-0497 with Dr K.-H. Kim as technical monitor. Computing resources were provided by the Arctic Region Supercomputing Center of HPCMP and the Minnesota Supercomputing Institute.

REFERENCES

ARAKERI, V. H. 1975 Viscous effects on the position of cavitation separation from smooth bodies. *J. Fluid Mech.* **68** (4), 779–799.

ARAKERI, V. H. & ACOSTA, A. J. 1973 Viscous effects in the inception of cavitation on axisymmetric bodies. *Trans. ASME J. Fluids Engng* **95** (4), 519–527.

ARNDT, R. E. A. 2002 Cavitation in vortical flows. *Annu. Rev. Fluid Mech.* **34** (1), 143–175.

ARNDT, R. E. A. & MAINES, B. H. 2000 Nucleation and bubble dynamics in vortical flows. *Trans. ASME J. Fluids Engng* **122** (3), 488–493.

ARNDT, R. E. A., SONG, C. C. S., KJELDSEN, M., HE, J. & KELLER, A. 2000 Instability of partial cavitation: a numerical/experimental approach. In *Proceedings of the 23rd Symposium on Naval Hydrodynamics*, pp. 519–615. National Academies Press.

BALACHANDAR, R. & RAMAMURTHY, A. S. 1999 Pressure distribution in cavitating circular cylinder wakes. *J. Engng Mech.* **125** (3), 356–358.

BEARMAN, P. W. 1969 On vortex shedding from a circular cylinder in the critical Reynolds number regime. *J. Fluid Mech.* **37** (3), 577–585.

BELAHADJI, B., FRANC, J.-P. & MICHEL, J.-M. 1995 Cavitation in the rotational structures of a turbulent wake. *J. Fluid Mech.* **287**, 383–403.

BRANDNER, P. A., WALKER, G. J., NIEKAMP, P. N. & ANDERSON, B. 2010 An experimental investigation of cloud cavitation about a sphere. *J. Fluid Mech.* **656**, 147–176.

COLONIUS, T. 2004 Modeling artificial boundary conditions for compressible flow. *Annu. Rev. Fluid Mech.* **36**, 315–345.

COUTIER-DELGOSHA, O., STUTZ, B., VABRE, A. & LEGOUPIL, S. 2007 Analysis of cavitating flow structure by experimental and numerical investigations. *J. Fluid Mech.* **578**, 171–222.

DIPANKAR, A., SENGUPTA, T. K. & TALLA, S. B. 2007 Suppression of vortex shedding behind a circular cylinder by another control cylinder at low Reynolds numbers. *J. Fluid Mech.* **573**, 171–190.

FRANC, J.-P. & MICHEL, J.-M. 1985 Attached cavitation and the boundary layer: experimental investigation and numerical treatment. *J. Fluid Mech.* **154**, 63–90.

FRANC, J.-P. & MICHEL, J.-M. 1988 Unsteady attached cavitation on an oscillating hydrofoil. *J. Fluid Mech.* **193**, 171–189.

FRY, S. 1984 Investigating cavity/wake dynamics for a circular cylinder by measuring noise spectra. *J. Fluid Mech.* **142**, 187–200.

GERRARD, J. H. 1966 The mechanics of the formation region of vortices behind bluff bodies. *J. Fluid Mech.* **25** (2), 401–413.

GNANASKANDAN, A. & MAHESH, K. 2014 Large eddy simulation of sheet to cloud cavitation. In *Proceedings of the 30th Symposium on Naval Hydrodynamics*, pp. 1–13.

GNANASKANDAN, A. & MAHESH, K. 2015 A numerical method to simulate turbulent cavitating flows. *Intl J. Multiphase Flow* **70**, 22–34.

HAMMACHE, M. & GHARIB, M. 1991 An experimental study of the parallel and oblique vortex shedding from circular cylinders. *J. Fluid Mech.* **232**, 567–590.

HSIAO, C.-T. & CHAHINE, G. L. 2005 Scaling of tip vortex cavitation inception noise with a bubble dynamics model accounting for nuclei size distribution. *Trans. ASME J. Fluids Engng* **127** (1), 55–65.

KATZ, J. 1982 Cavitation inception in seperated flows. PhD thesis, California Institute of Technology.

KATZ, J. 1984 Cavitation phenomena within regions of flow separation. *J. Fluid Mech.* **140**, 397–436.

KUBOTA, A., KATO, H. & YAMAGUCHI, H. 1992 A new modelling of cavitating flows: a numerical study of unsteady cavitation on a hydrofoil section. *J. Fluid Mech.* **240**, 59–96.

KUNZ, R. F., BOGER, D. A., STINEBRING, D. R., CHYCZEWSKI, T. S., LINDAU, J. W., GIBELING, H. J., VENKATESWARAN, S. & GOVINDAN, T. R. 2000 A preconditioned Navier–Stokes method for two-phase flows with application to cavitation prediction. *Comput. Fluids* **29** (8), 849–875.

LABERTEAUX, K. R. & CECCIO, S. L. 2001 Partial cavity flows. Part 1. Cavities forming on models without spanwise variation. *J. Fluid Mech.* **431**, 1–41.

MATSUDAIRA, Y., GOMI, Y. & OBA, R. 1992 Characteristics of bubble-collapse pressures in a Karman-vortex cavity. *JSME Intl J.* **35** (2), 179–185.

MITTAL, S. & RAGHUVANSHI, A. 2001 Control of vortex shedding behind circular cylinder for flows at low Reynolds numbers. *Intl J. Numer. Meth. Fluids* **35** (4), 421–447.

PARK, N. & MAHESH, K. 2007 Numerical and modeling issues in LES of compressible turbulence on unstructured grids. In *Proceedings of the 45th AIAA Aerospace Sciences Meeting and Exhibit, AIAA Paper*, pp. 1–18.

RAMAMURTHY, A. S. & BHASKARAN, P. 1977 Constrained flow past cavitating bluff bodies. *Trans. ASME J. Fluids Engng* **99** (4), 717–726.

RAO, B. C. S. & CHANDRASEKHARA, D. V. 1976 Some characteristics of cavity flow past cylindrical inducers in a venturi. *Trans. ASME J. Fluids Engng* **98** (3), 461–466.

RAO, B. C. S., CHANDRASEKHARA, D. V. & SEETHARAMIAH, K. 1972 A high-speed photographic study of vortex shedding behind circular cylinders of cavitating flows. In *Proceedings of 2nd International JSME Symposium Fluid Machinery and Fluidics*, pp. 293–302.

ROSHKO, A. 1961 Experiments on the flow past a circular cylinder at very high Reynolds number. *J. Fluid Mech.* **10** (3), 345–356.

ROUSE, H. & MCNOWN, J. S. 1948 Cavitation and pressure distribution: head forms at zero angle of yaw. *State University of Iowa, Studies in Engineering, Bulletin* 32. Published by the State University of Iowa.

SAITO, Y. & SATO, K. 2003 Cavitation bubble collapse and impact in the wake of a circular cylinder. In *Proceedings of the 5th International Symposium on Cavitation*, pp. 1–6.

SAITO, Y., TAKAMI, R., NAKAMORI, I. & IKOHAGI, T. 2007 Numerical analysis of unsteady behavior of cloud cavitation around a NACA0015 foil. *Comput. Mech.* **40** (1), 85–96.

SCHMIDT, S. J., SCHNERR, G. & THALHAMER, M. 2009 Inertia controlled instability and small scale structures of sheet and cloud cavitation. In *Proceedings of the 7th International Symposium on Cavitation*, pp. 1–14.

SCHNERR, G. H., SEZAL, I. H. & SCHMIDT, S. J. 2008 Numerical investigation of three-dimensional cloud cavitation with special emphasis on collapse induced shock dynamics. *Phys. Fluids* **20** (4), 1–9.

SELIM, S. M. 1981 Cavitation erosion in fluid flow. PhD thesis, University of Southampton.

SENOCAK, I. & SHYY, W. 2002 A pressure-based method for turbulent cavitating flow computations. *J. Comput. Phys.* **176** (2), 363–383.

SEO, J. H., MOON, Y. J. & SHIN, B. R. 2008 Prediction of cavitating flow noise by direct numerical simulation. *J. Comput. Phys.* **227** (13), 6511–6531.

SHIN, B. R., IWATA, Y. & IKOHAGI, T. 2003 Numerical simulation of unsteady cavitating flows using a homogenous equilibrium model. *Comput. Mech.* **30** (5–6), 388–395.

SINGHAL, A. K., ATHAVALE, M. M., LI, H. & JIANG, Y. 2002 Mathematical basis and validation of the full cavitation model. *Trans. ASME J. Fluids Engng* **124** (3), 617–624.

STRYKOWSKI, P. J. & SREENIVASAN, K. R. 1990 On the formation and suppression of vortex shedding at low Reynolds numbers. *J. Fluid Mech.* **218**, 71–107.

VARGA, J. J. & SEBESTYEN, G. Y. 1972 Determination of hydrodynamic cavitation intensity by noise measurement. In *Proceedings of the 2nd International JSME Symposium on Fluid Machinery and Fluidics*, pp. 285–292.

VERMA, A. & MAHESH, K. 2012 A Lagrangian subgrid-scale model with dynamic estimation of Lagrangian time scale for large eddy simulation of complex flows. *Phys. Fluids* **24** (8), 85–101.

WILLIAMSON, C. H. K. 1988 Defining a universal and continuous Strouhal–Reynolds number relationship for the laminar vortex shedding of a circular cylinder. *Phys. Fluids* **31** (10), 2742–2744.

WILLIAMSON, C. H. K. 1989 Oblique and parallel modes of vortex shedding in the wake of a circular cylinder at low Reynolds numbers. *J. Fluid Mech.* **206**, 579–627.

YEE, H. C., SANDHAM, N. D. & DJOMEHRI, M. J. 1999 Low-dissipative high-order shock-capturing methods using characteristic-based filters. *J. Comput. Phys.* **150** (1), 199–238.

YOUNG, J. O. & HOLL, J. W. 1966 Effects of cavitation on periodic wakes behind symmetric wedges. *Trans. ASME J. Fluids Engng* **88** (1), 163–176.